Radiation Physics and Chemistry 238 (2026) 113162

Contents lists available at ScienceDirect

Radiation Physics and Chemistry

journal homepage: www.elsevier.com/locate/radphyschem

The energy lost by α-particles from ^{241}Am in Al, Cu, Sn, and Au films: Measurements with 0.7% accuracy and first-principles calculations

A. Mangiarotti [a,*], A.A. Malafronte [a], A.R. Petri [a,1], M.N. Martins [a], J.M. Fernández-Varea [b,c], J.P. Peralta [d], A.M.P. Mendez [d], D.M. Mitnik [d], C.C. Montanari [d]

[a] Instituto de Física da Universidade de São Paulo, Rua do Matão 1371, 05508-090 São Paulo, Brazil
[b] Departament de Física Quàntica i Astrofísica, Universitat de Barcelona, Martí i Franquès 1, ES-08028, Barcelona, Catalonia, Spain
[c] Institut de Ciències del Cosmos (ICCUB), Universitat de Barcelona, Martí i Franquès 1, ES-08028, Barcelona, Catalonia, Spain
[d] Instituto de Astronomía y Física del Espacio, CONICET and Universidad de Buenos Aires, Buenos Aires, Argentina

ARTICLE INFO

Keywords:
Energy loss
α-particles
Metallic films
SRIM
ASTAR
Shellwise local plasma approximation

ABSTRACT

The energies lost, ΔE_1, by the α-particles from ^{241}Am in Al, Cu, Sn, and Au metallic targets have been measured. The films are not thin enough to extract a stopping cross section because they have to withstand the independent determination of their mass thickness $\rho x_0 = \Delta m/\Delta A$ through their weights Δm and surfaces ΔA. The systematic uncertainties on ΔE_1 (including the ones on ρx_0) are estimated to be 0.6–0.7%. The largest contribution of 0.33% comes from the long-term stability of the electronics. The uniformity and purity of the targets have smaller impacts. The effect of the former, in particular, is attenuated by the diameter of the collimator of 6.5 mm. A correction for the average track inclination of 0.1% is applied. All the runs lasted enough to reduce the combined statistical errors to $\approx 0.1\%$, which becomes irrelevant for the comparison with theory. The largest deviation of the experimental ΔE_1 from the predictions of ASTAR is -0.3% for Cu. The situation is less regular for SRIM with a discrepancy of up to -2.0% also for Cu. First-principles calculations without any free parameters have also been carried out within the shellwise local plasma approximation (SLPA-LM). This formalism relies exclusively on fundamental atomic properties not directly related to particle stopping.

1. Introduction

The investigations about the penetration of α-particles into matter begun at the dawn of the discovery of radioactivity, notably, dating back to the pioneering works by Curie (1900), by sir William Henry Bragg together with Richard Kleeman (Bragg and Kleeman, 1905, 1904), and by sir Rutherford (1906). The efforts never waned up to the present days producing a huge amount of data. A global drive, under the auspices of the International Atomic Energy Agency (IAEA), has recently taken over the task to produce a comprehensive database (Montanari and Dimitriou, 2017; Montanari et al., 2024; Montanari, 2025). Our own assessment of the situation after 1990 is presented in Section 2. It looks remarkably different from the one typical of other areas, see e.g. Fig. 1 of the Particle Data Group (PDG) report (Navas et al., 2022). In fact, no real tendency of the results to settle around accepted values can be clearly identified. Discrepancies of up to several tens of percent are easily encountered amongst different groups of authors. Such a feature is possibly connected to the non-elementary nature of the process at hand. We try to contribute by reporting measurements of the energy ΔE_1 lost by the most energetic α-particles from ^{241}Am ($E_1 = (5.48556 \pm 0.00012)$ MeV) in Al, Cu, Sn, and Au metallic films. A detailed investigation of the statistical and systematic uncertainties is a mandatory part of the task. We estimate the latter to be dominant and quantify their total impact at 0.7% in the worst case. The targets are not thin enough to allow for a direct determination of the stopping power. This is the price to pay to have absolute values (i.e. not relative to those of other particle species) because the films must be robust enough to withstand a direct determination of their weight Δm and area ΔA for finding out their mass thickness $\rho x_0 = \Delta m/\Delta A$ (with ρ the mass density of the material).

Two of the most widely-spread semi-empirical approaches (ASTAR Berger et al., 1993 and SRIM Ziegler et al., 1985; Ziegler, 2004; Ziegler et al., 2010) predict well the experimental ΔE_1 (although the former has a more consistent overall performance). However, they

* Corresponding author.
E-mail address: alessio@if.usp.br (A. Mangiarotti).
[1] Now at INFN, Sez. Milano.

https://doi.org/10.1016/j.radphyschem.2025.113162
Received 19 May 2025; Received in revised form 3 July 2025; Accepted 7 July 2025
Available online 17 July 2025

both extract their parameters (most notably the mean excitation energy I) from stopping power data themselves, albeit for protons. A recent improvement (`cbethe` Salvat et al., 2022; Salvat, 2022) with the shell correction evaluated from realistic Dirac–Hartree–Fock–Slater wave functions is also analysed. The advancement of theory is, however, most appropriately probed by first-principles calculations. Here we consider the so-called shellwise local plasma approximation (SLPA-LM) (Montanari and Miraglia, 2013; Peralta et al., 2022, 2023) in its most recent variant employing the Levine–Mermin dielectric response function (Mermin, 1970; Levine and Louie, 1982) for the bound electrons (Peralta et al., 2022). It is noteworthy because it relies exclusively on the atomic radial wave functions and shell binding energies, which are quantities not directly related to the passage of particles through matter, supplemented by a damping constant.

The energy loss of α-particles crossing various materials is an important topic in many areas of pure and applied sciences like astrophysics (Moroz et al., 2004), plasma physics (Salonen et al., 2000), and materials engineering (Zinkle et al., 2002). We remind, to those who may find the present pursuit of precision excessive, that the setup and analysis procedures described in the present work were developed to validate the determination of the target thicknesses in high-energy (500 MeV) bremsstrahlung experiments. The uncertainties have to be small enough for the data to be sensitive to the presence of higher-order terms in the asymptotic value of the Coulomb correction (Mangiarotti et al., 2021a).

It is convenient to spell out here the conventions followed in the rest of the exposition. The modulus of the stopping force or stopping power is indicated as $S = -dE/dx$. We avoid, except for making an essential point in Section 4.5, recourse to the mass stopping power S/ρ and prefer instead the stopping cross section (SCS) $\mathcal{E} = S/\mathcal{N}$, where $\mathcal{N}$ is the number density of the substance.

The paper is organized as follows. The consistency of the available SCS data is assessed in Section 2. The experimental method and the data analysis procedures are described in Sections 3 and 4, respectively. Particular emphasis is given to the estimation of the systematic uncertainties in Section 4.5. The SLPA-LM model is reviewed in Section 5. Theories are confronted with measurements in Section 6. Finally, our conclusion is offered in Section 7.

2. Status of the available measurements

The current status of SCS measurements can be assessed by resorting to the IAEA database (Montanari and Dimitriou, 2017; Montanari et al., 2024; Montanari, 2025), an up-to-date collection of published results based on an earlier version initiated by Helmut Paul (2003). Experiments with α-particles penetrating Sn have been reported before by 6 works. In all the other cases, many more datasets are available, although some are rather old going back to the 1960s. Judging the best of them is a well-known problem with essentially no accepted solution, actually motivating the very existence of the IAEA database. Yet, a diffuse cloud of points will result from accepting all the entries. Hence, we adopted a simple chronological criterion, filtering out those that appeared before 1990. Although most recent does not necessarily means better. The comparisons are displayed in Fig. 1. The energy range considered is from 1.0 keV to 1.0 GeV because it is covered by both the tables of the ICRU Report 49 (Berger et al., 1993) (ASTAR) and the SRIM programs (Ziegler et al., 1985; Ziegler, 2004; Ziegler et al., 2010). The former is also available as part of the NIST Standard Reference Database Number 124 (Berger et al., 2017). The variation of the SCSs spans about two orders of magnitude so that differences of several percent can hardly be appreciated on a linear or log scale. Thus, we preferred to plot the percentage deviation with respect to the ASTAR expectation, anticipating the conclusions of Section 6. The correspondence between the letter key employed in Fig. 1 and the original reference is given in Table 1. The dots represent the calculations with SRIM version 2013 (Ziegler et al., 2010).

Table 1
References to the original publications in the IAEA database (Montanari and Dimitriou, 2017; Montanari et al., 2024; Montanari, 2025) for the SCSs of α-particles in Al, Cu, Sn, and Au appeared after 1990 (included). The data are displayed in Fig. 1 according to the keys.

Key	Al
a	Räisänen et al. (1991)
b	Sakamoto et al. (1991)
c	Eppacher (1994)
d	Martínez-Tamayo et al. (1996)
e	Bianconi et al. (2005)
f	Hsu et al. (2005)
g	Hsu et al. (2005)
h	Primetzhofer et al. (2011)
i	Diwan and Kumar (2015)
j	Moussa et al. (2015)
k	Trzaska et al. (2018)
Key	**Cu**
a	Sakamoto et al. (1991)
b	Bak et al. (1994)
c	Sillanpää et al. (1996)
d	Markin et al. (2009)
Key	**Sn**
a	Räisänen et al. (1991)
b	Sakamoto et al. (1991)
c	Eppacher (1994)
d	Kumar and Diwan (2015)
Key	**Au**
a	Semrad et al. (1990)
b	Sakamoto et al. (1991)
c	Eppacher (1994)
d	Bak et al. (1994)
e	Martínez-Tamayo et al. (1996)
f	Trzaska et al. (2002)
g	Hsu et al. (2004)
h	Hsu et al. (2004)
i	Zhang et al. (2005)
j	Markin (2007)
k	Markin et al. (2009)
l	Primetzhofer (2012)
m	Kumar and Diwan (2018)
n	Trzaska et al. (2018)

The discrepancies between different authors increase widely up to ≈40% below ≈100 keV, as it is visible from Fig. 1. This is certainly due to increasing experimental difficulties to work at low energies. Sets j, k, and l for Au (see Table 1) deserve to be mentioned explicitly since they established the breakdown of the velocity proportionality for very slow ions and the H/He anomaly. Both features were explained by refined *ab initio* calculations with the real-time time-dependent density functional theory (RT-TDDFT) (Ahsan Zeb et al., 2012; Correa, 2018). These experiments are reasonably well reproduced by SRIM but not by ASTAR. Unfortunately, the present study is restricted to energies about two orders of magnitude higher and we cannot contribute much to such an interesting discussion. However, even in the few MeV region here contemplated, differences of up to ≈±10% do exist (compare sets a, g, and f in Al or f, h, and m in Au). Predictions from the RT-TDDFT approach are available up to 3.5 MeV (Ullah et al., 2018) for Ni ions in a Ni target suggesting SRIM values are too high by a similar figure of ≈10%. It is correspondingly not possible to rely on SCS calculations at a level of ≈0.5% without a direct experimental confirmation.

The ASTAR and SRIM approaches tend to agree very well at high energies while large deviations build-up at low ones. They are both similar in general terms, being based on the Bethe–Bloch formula with Bloch, Barkas–Andersen, shell, and density-effect corrections (Berger et al., 1993) above a few MeV. The needed parameters are extracted from a fit to the data: it is, thus, correct to term the method as semi-empirical. Approximated expressions, inspired by the Varelas and Biersack (1970) one, are adopted in the low-energy region with various

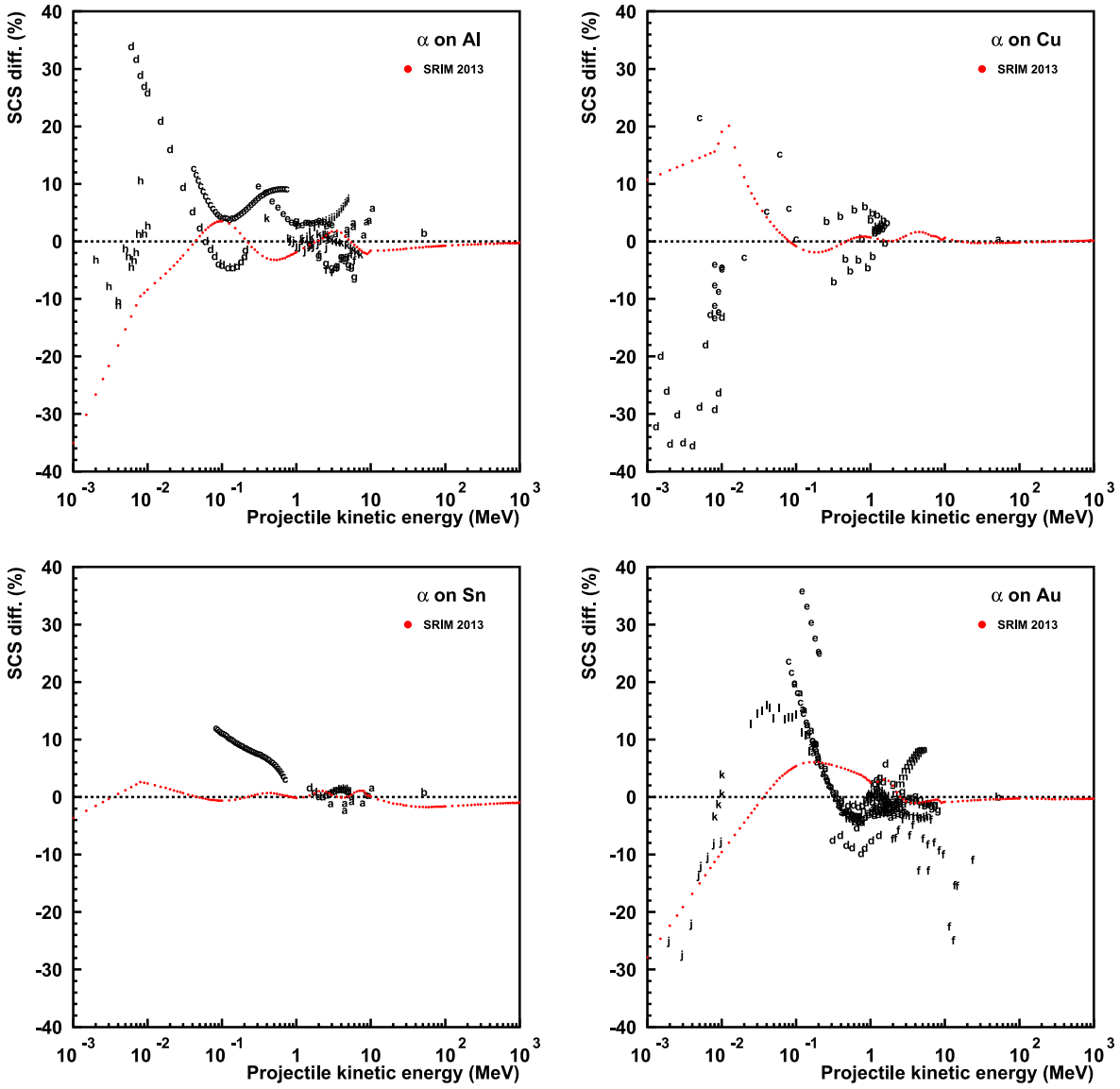

Fig. 1. Available SCS measurements of Al, Cu, Sn, and Au for α-particles (He ions) taken from the IAEA database (Montanari and Dimitriou, 2017; Montanari et al., 2024; Montanari, 2025) published from 1990. The keys are associated to the references in Table 1. The smooth behaviour predicted by the ICRU Report 49 (Berger et al., 1993) has been subtracted to ease the visualization of the discrepancies through the relative differences, reported on the vertical scale. The results of SRIM version 2013 are plotted as (red) dots.

procedures followed to achieve a smooth merge with the Bethe–Bloch formula. The latter part is clearly subject to larger difficulties as SRIM deviates from ASTAR by up to ≈40%, as mentioned above.

3. Experiment

The experimental setup is rather simple but great care has been exercised during each step, as well as in the characterization of the targets.

3.1. Preparation of the targets

The Cu, Sn, and Au targets used in the energy-loss measurements have been prepared from commercial-grade films manufactured by Goodfellow.[2] The purchased foils have a nominal area of 25 × 25 mm^2 and a nominal thickness of 2.5 μm.[3] They were all of the NLT grade. It is our understanding that the LT (light tight) and NLT (not light tight) types are essentially from the same production line, the LT ones being selected by Goodfellow through visual inspection. The LT types are more expensive, not readily available on the shelves to be purchased and, more importantly, not guaranteed by Goodfellow to have superior thickness uniformity. Therefore, we decided to purchase the NLT variant and make our own selection at the moment of choosing the part of the film to be employed. A portion amounting approximately to one quarter of each foil has been cut to be later glued onto a rectangular frame made of stainless steel. This support has dimensions of 15 × 30 mm^2, a thickness of 0.5 mm, and a circular hole in the centre with a diameter of 10 mm. A few very small holes can easily be

[2] Goodfellow Cambridge Ltd., the product catalogue is available from their web site at https://www.goodfellow.com.

[3] The Goodfellow catalogue numbers are CU000120 323-963-95, SN000070 823-443-15, and AU000080 722-905-05 for the Cu, Sn, and Au foils, respectively.

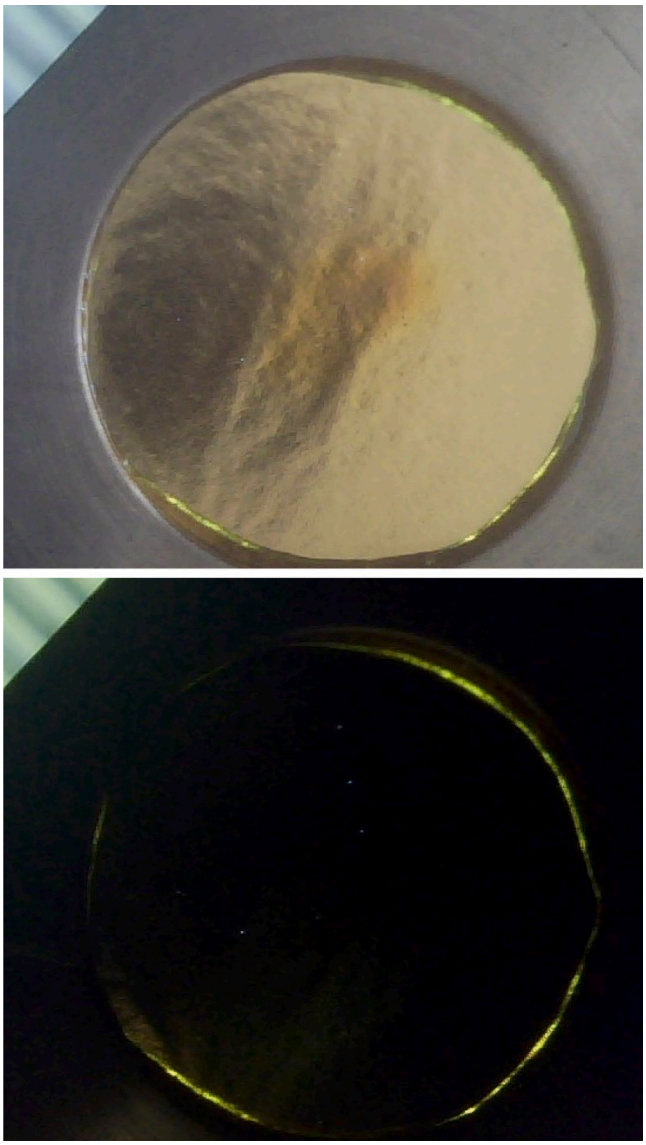

Fig. 2. Pictures of the Au target employed in the measurements. The upper and lower ones have been taken with front and backward illuminations, respectively. Five small holes can be easily spotted and then be found (with some patience) in the lower and upper panels, respectively.

spotted when the targets are back illuminated with a strong light. We have attempted to minimize their number both during the process of selecting the quarter of the foil to be cut and the orientation for gluing. Moreover, we have tried to position them away from the central region. The reader may gain a feeling of the overall results of the full procedure by inspecting the pictures of the Au target taken with both front and backward illumination. They are reproduced in the upper and lower panels of Fig. 2, respectively. The cases of the Sn and Au targets are similar, while no hole is visible in the Cu one.

The Al foil was borrowed from the Laboratório de Anlálise de Materiais por Feixes Iônicos (LAMFI) of the Institute of Physics of the University of São Paulo (IFUSP, Brazil). It is from the same roll characterized for the measurements of the SCSs for protons made at LAMFI by Moro et al. (2016). No holes could be identified in the Al target.

The determination of the foil thickness x_0 (or better the mass thickness $\rho\, x_0$) is of the same importance than that of the energy lost by the α-particles inside the target, since both enter on the same footing when a comparison to theory is attempted, see Section 6. It must be carried out before gluing onto the stainless steel frames. We found $\rho\, x_0$ by measuring separately the area ΔA and the mass Δm of the flake with a method very similar to that by Moro et al. (2016).

Table 2
Purity and average areal density $\mathcal{N}\, x_0 = N_A\, \rho\, x_0/\mathcal{M}$ (where N_A and $\mathcal{M}$ are the Avogadro constant and the molar mass, respectively) of the targets employed in the present work. The statistical, estimated as 1 standard deviation, and systematic uncertainties on $\mathcal{N}\, x_0$ are also given.

Target	Purity (mass %)	Areal density (10^{19} atoms/cm^2)	Stat. unc.	Syst. unc.
Al	98.78	3.311	0.002	0.007
Cu	99.97	1.941	0.002	0.004
Sn	99.76	1.261	0.002	0.003
Au	99.90	1.558	0.002	0.003

The area of the foils has been determined by taking images of them with a flatbed scanner model Perfection 610, manufactured by Epson®, selecting a resolution of 600 dpi. In this way, parallax errors have been avoided as compared to the method of making photos described by Moro et al. (2016). Ten images have been acquired of each foil in different positions and the ImageJ[4] software has been employed to extract their area. The necessary calibration of the flatbed scanner has been performed by collecting images of a stainless steel rule in the horizontal and vertical orientations. The average of the ten determinations of the area has a typical standard deviation of the order of 0.4–1 mm^2 or approximately 0.05%, 0.07%, 0.1%, and 0.1% for Al, Cu, Sn, and Au, respectively.

The foils have been weighted with a micro-analytic scale model XP6 manufactured by Mettler Toledo® and installed at the Laboratório de Física Atmosférica (LFA) of IFUSP. The process is delicate and care is needed (Reichmuth, 2001). The equipment is seated on a special masonry table, which is mechanically insulated from the walls of the building to avoid the transmission of vibrations. An air conditioning system is present in the room to stabilize the temperature and dry the air. The scale has been switched on long before its use to allow to reach steady operation (Reichmuth, 2001). The foils to be measured have also been left in the room for quite some time to reach equilibrium with the air (Reichmuth, 2001). Draft during weighing is reduced when the sample has the same temperature of the air (the XP6 has a draft shield built-in by the manufacturer as well). A radioactive source is positioned close to the scale to ionise the air, which becomes mildly conductive. The charge eventually accumulated on the foils during the positioning on the weighting pan can then easily disperse. Five measurements have been taken for each foil, in different positions on the weighing pan, to check the overall reproducibility. This is also important to verify the absence of any charging-up effects (Reichmuth, 2001). The average has a typical standard deviation of ≈1 μg corresponding to approximately 0.003%, 0.01%, 0.02%, and 0.006% in Al, Cu, Sn, and Au, respectively. Since these values are smaller than the correction for the air buoyancy, we have taken it into account using the nominal mass densities (Reichmuth, 2001).

Combining the areas and the weights results in the areal densities of Table 2. The statistical uncertainties given in the 4th column (1 standard deviation) are the outcome of the error propagation from the measured quantities. The relative contribution of the uncertainty on the area is ≈5 to 17 times that of the mass. The correction for the air buoyancy becomes, therefore, unimportant for all targets except Al, where it changes $3.310 \cdot 10^{19}$ to $3.311 \cdot 10^{19}$ atoms/cm^2 (see Table 2). The systematic errors, also listed in Table 2 (5th column), are discussed in

[4] ImageJ is an image processing program, written in Java. It was developed jointly by the National Institutes of Health and the Laboratory for Optical and Computational Instrumentation of the University of Wisconsin. More information can be found at https://imagej.net/ij/index.html.

Section 4.5. The result for the Al target agrees with that given by Moro et al. (2016) within ≈3%, which is ≈10 times the uncertainties estimated combining those of Table 2 with the ones by Moro et al. (2016). This difference gives an idea of the large-scale uniformity of the roll (as a figure of reference, Goodfellow grants a maximum batch to batch variation of ±25% for thicknesses below 0.010 mm).

The impurities in the Al foil have been studied employing Rutherford Backscattering Spectrometry (RBS) by Moro et al. (2016) revealing the presence of C, O, Fe, Mn, and Zn with atomic percentage abundances of (0.986 ± 0.064)%, (0.687 ± 0.058)%, (0.13013 ± 0.0041)%, (0.0341 ± 0.0010)% and (0.0098 ± 0.0021)%, respectively. The corresponding purity is quoted in Table 2 as a percentage by mass, assuming it applies to the whole roll. No RBS investigations have been conducted for the Cu, Sn, and Au targets. The purities ensured by Goodfellow are provided in Table 2. Moreover, the supplier reports a typical analysis listing the elemental composition down to 1 ppm in mass. The targets have been kept in special vacuum chambers (larger ones for permanent storage and smaller ones for transportation), after their production, in order to slow down the natural oxidation process in air as well as the deposition of contaminants and moisture.

3.2. Radioactive sources

The ^{241}Am source (model AMR.22 manufactured by Amersham®) was produced by chemical deposition on a copper disk. The layer of radioactive isotope is very thin to avoid any energy loss of the emitted α-particles but, for the same reason, the activity ends up being low: it was ≈525 Bq during the measurements. The minimization of the energy lost by the α-particles inside the source is, however, of paramount importance for the success of the measurements because it directly competes with the energy lost in the target foils.

The ^{232}Th source is actually a natural thorium target left over from a previous experiment. It was manufactured by electrodeposition on an aluminium film fixed on a rigid frame.

3.3. Experimental setup

The energy of the α-particles is measured with a Passivated Implanted Planar Silicon (PIPS®) detector model PD100-14-300AM manufactured by Canberra®. It is of the partially-depleted type, meaning that the Si wafer is thicker than the depletion zone, with the connector mounted axially. The active area is 100 mm^2. The manufacturer states a depletion region thickness of 300 μm, at the nominal reverse bias voltage of 40 V, and a nominal energy resolution of 14 keV (FWHM) for the α-particles from ^{241}Am.

The setup consists essentially of a radioactive source, a collimation system, a target insertion device, and the detector, see Fig. 3. The ^{241}Am and ^{232}Th sources have a low activity, as mentioned, and some care has to be exercised to avoid a too narrow beam that may decrease the counting rate excessively. The collimator is made by two holes, drilled in two aluminium plates, with a diameter of 6.5 mm separated by a distance of 43 mm, see again Fig. 3. The two plates are actually connected on two opposite ends to form a box-shaped structure. The source is suspended quite close to the entrance of the collimator. The ^{241}Am deposition, see Section 3.2, has the shape of a disk whose diameter is ≈7 mm, matching that of the hole. The target is held immediately behind the exit of the collimator, and the detector closely above the target so as to avoid any unnecessary geometrical loss of α-particles (Monte Carlo estimates are introduced in Section 4.4). Moreover, the use of as-open-as-possible apertures in the collimator allows to average the measured lost energy over a large fraction of the target reducing the impact of non-uniformities (see Section 4.5). The mean track inclination is still small in the current setup and is corrected for (see Section 4.4). The complete system is mounted inside a vacuum chamber connected to a turbomolecular pump. The air pressure has been maintained below ≈7 mPa during the measurements.

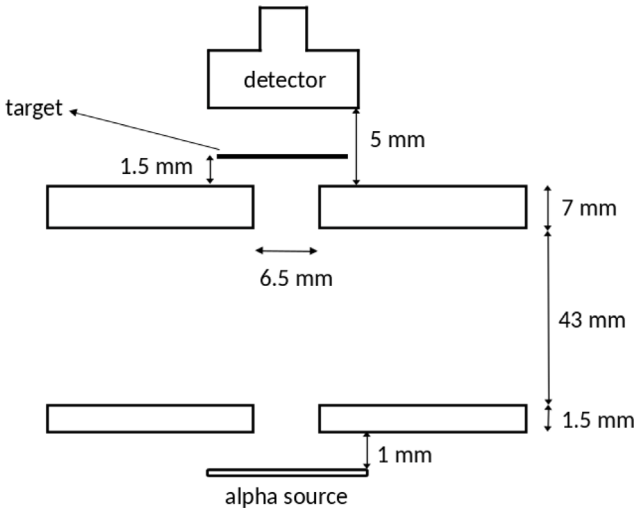

Fig. 3. Cut view of the experimental setup. The source-collimator-detector axis belongs to the plane of the figure, which is also perpendicular to the aluminium lids forming the collimator.

The electronics read-out chain consists of a 142IH preamplifier, a 572 shaping amplifier, and a 927 Aspec peak sensing ADC, all manufactured by Ortec®. The PD100-14-300AM is reverse biased at 40 V by a 710 power supply, also manufactured by Ortec®. The cable connecting the PIPS detector with the 142IH has been kept as short as possible with a total length of ≈30 cm and a vacuum feedthrough more or less in the middle. The gain of the 572 amplifier has been set to 30 and the shaping time to 2 μs. All acquisitions have been made with 8192 channels. Typical runs lasted between one and two days.

4. Data analysis

A precise energy calibration is of foremost importance to obtain accurate energy-loss values. The response function (RF) of the PIPS detector is not well approximated by a simple Gaussian for monoenergetic α-emission lines in absence of any target. Therefore, a better fitting model had to be devised. When the analysis is implemented well, only the slope of the energy calibration enters into the determination of the lost energy ΔE_1, i.e. the displacement of the most intense peak from ^{241}Am when the target is inserted with respect to the no-target condition. The calibration process must cover, to ensure reliable results, both the energy of the direct ^{241}Am peaks as well as the lower ones reached after the α-particles cross the targets. We have decided to employ the ^{232}Th source because it was readily available and well suited to the task.

4.1. Detector response function

The RF of a planar silicon detector to monoenergetic α-particles is rather complex. This has been widely known for the older silicon barrier devices since the pioneering studies by L'Hoir (1984) (see also the other references given by him to his prior publications). It is also the case for the modern PIPS ones relied upon in the present work. In particular, the RF has an asymmetric tail towards lower detected energies mostly due to energy-loss straggling in the thin passive entrance layer and incomplete charge collection. L'Hoir (1984) proposed to model such a skewed peak using the convolution (Brandt, 2014)

$$h(E,E_0)=\int_{-\infty}^{E_0} \mathrm{d}E\, f(E',E_0)\,\frac{1}{\sqrt{2\pi}\,\sigma}\,\exp\left(-\frac{(E-E')^2}{2\,\sigma^2}\right) \tag{1}$$

of a Gaussian with a one-sided exponential

$$f_{\mathrm{LH}}(E,E_0)=\frac{1}{d}\,\exp\left(\frac{E_0-E}{d}\right)\Theta(E_0-E)\ , \tag{2}$$

where E_0 is the fixed energy of the incident α-particles, σ the standard deviation of the Gaussian, Θ the Heaviside unit-step function, and d the characteristic energy scale of the exponential tail. As a matter of fact, such a procedure implicitly assumes that there are two statistically independent sources of fluctuations: one corresponding to a symmetric smearing (e. g. electronic noise and division between electronic and nuclear energy loss in the active detector) and another one to an asymmetric distribution favouring large losses (e. g. incomplete charge collection and energy-loss straggling in the entrance passive layer). The convolution of Eq. (1) with the expression of Eq. (2) can be carried out analytically arriving at

$$\begin{aligned} h_{\mathrm{LH}}(E,E_0)=&\frac{1}{2\,d}\,\exp\left(\frac{E-E_0}{d}+\frac{\sigma^2}{2\,d^2}\right)\\ &\times\,\mathrm{erfc}\left(\frac{1}{\sqrt{2}}\left(\frac{E-E_0}{\sigma}+\frac{\sigma}{d}\right)\right)\ , \end{aligned} \tag{3}$$

where erfc is the complementary error function (Abramowitz and Stegun, 1972).

Note that the extension of the lower limit of integration in Eq. (1) down to $-\infty$, as well as the normalization of the exponential in Eq. (2) in the interval $(-\infty, E_0)$, is not fully consistent because, in reality, a deposited negative energy has no meaning. The expressions consistently considering the range $(0, E_0)$ are given by Mangiarotti et al. (2021b). Nevertheless, as justified there, the use of this more correct approach is relevant only if it is desired to describe the RF down to a lowest recorded energy threshold which is close to zero. Here, we are rather interested in the region of the spectrum close to the α-particle emission lines and, therefore, this further simplification is acceptable.

The non-dimensional quantity $\tau = d/\sigma$ is useful, as found by L'Hoir (1984), to characterize the distribution from Eq. (3). In particular, when $\tau \ll 1$, Eq. (3) is well approximated by a Gaussian. On the other hand, Eq. (3) is quite close to an exponential when $\tau \gg 1$.

It has, however, also been well known that Eq. (3) is not fully adequate to describe the RF of a planar silicon detector to monoenergetic α-particles especially when using very thin sources: Bortels and Collares (1987) proposed to adopt the convolution with a Gaussian of two (or three) one-sided exponentials plus a constant. Our experience is, indeed, that Eq. (3) is not fully satisfactory for the thin ^{241}Am source employed (see Section 3.2). Moreover, it is necessary to pay attention to the value of τ for each exponential introduced. When the fit results in a short-range exponential (i. e. $\tau \ll 1$), it becomes unstable due to the reduced sensitivity to d. We attempted to simplify the RF proposed by Bortels and Collares (1987) considering the convolution with a Gaussian of a Dirac δ-function plus two one-sided exponentials

$$\begin{aligned} f_{\mathrm{sBC}}(E,E_0)=&(1-w_1-w_2)\,\delta(E-E_0)\\ &+\,w_1\,\frac{1}{d_1}\,\exp\left(\frac{E_0-E}{d_1}\right)\Theta(E_0-E)\\ &+\,w_2\,\frac{1}{d_2}\,\exp\left(\frac{E_0-E}{d_2}\right)\Theta(E_0-E)\ , \end{aligned} \tag{4}$$

where d_1 and d_2 are the characteristic energy scales of the exponential tails, while w_1 and w_2 are the relative areas of their contributions. We refer to Eq. (4) as "sBC" standing for simplified Bortels and Collares. The proposed Eq. (4) is also based on our previous experience with electrons (Mangiarotti et al., 2021b). The convolution of a Gaussian, see Eq. (1), with the expression of Eq. (4) can be done analytically,

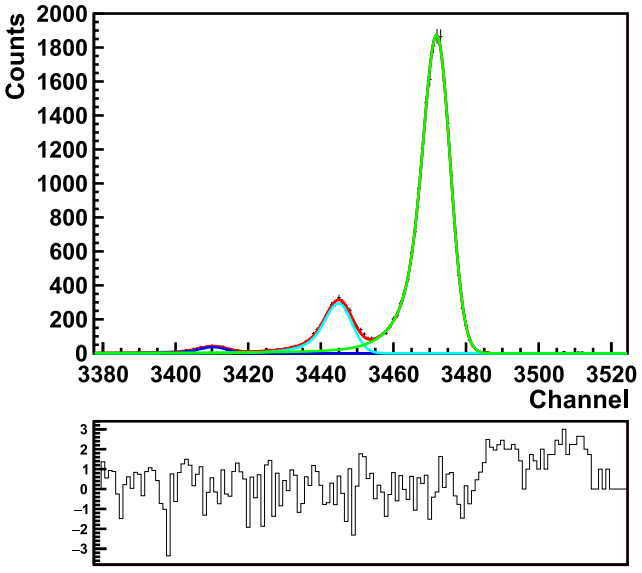

Fig. 4. Spectrum from the ^{241}Am source. The fit (red curve) relied on the RF from Eq. (5), as described in the text. The contribution from each of the three α-lines are also plotted (green, cyan, and blue curves). The lower panel provides the ratio of the deviation from the fitted function to the statistical error for each bin.

yielding

$$\begin{aligned} h_{\mathrm{sBC}}(E,E_0)=&(1-w_1-w_2)\,\frac{1}{\sqrt{2\pi}\,\sigma}\,e^{-\frac{(E-E_0)^2}{2\sigma^2}}\\ &+\,\frac{w_1}{2\,d_1}\,\exp\left(\frac{E-E_0}{d_1}+\frac{\sigma^2}{2\,d_1^2}\right)\\ &\times\,\mathrm{erfc}\left(\frac{1}{\sqrt{2}}\left(\frac{E-E_0}{\sigma}+\frac{\sigma}{d_1}\right)\right)\\ &+\,\frac{w_2}{2\,d_2}\,\exp\left(\frac{E-E_0}{d_2}+\frac{\sigma^2}{2\,d_2^2}\right)\\ &\times\,\mathrm{erfc}\left(\frac{1}{\sqrt{2}}\left(\frac{E-E_0}{\sigma}+\frac{\sigma}{d_2}\right)\right)\ . \end{aligned} \tag{5}$$

We have adopted Eq. (5) for the very thin ^{241}Am source, Eq. (3) for the thicker ^{232}Th source, and a simple Gaussian when the target is inserted. Each is, of course, multiplied by an overall normalization factor before executing the fits described in the next subsections. They have been made with the C++ reimplementation of the MINUIT package (James and Roos, 1975) contained in the ROOT data analysis framework (Brun and Rademakers, 1997) by searching for the minimum of the Pearson-χ^2 (Baker and Cousins, 1984). Such a choice of a merit function avoids any difficulties with empty channels because the uncertainty in the content of each histogram bin is estimated from the square root of the fitted function.

4.2. Energy calibration

The calibration process relies on the accepted energies and branching ratios of α-emission lines. In fact, they are known with a precision far greater than the uncertainties associated with the present setup, being the subject of metrological publications (Bé et al., 2004).

The energy spectrum collected with the ^{241}Am source is reproduced in Fig. 4. We have first-hand experienced the inadequacy of Eq. (3) to describe the data, as is well recognised in the published literature (Bortels and Collares, 1987). The fit has, afterwards, been made applying Eq. (5). It is shown as well in Fig. 4. Indeed, the source is thin resulting in small energy losses of the escaping α-particles and, consequently, the low-energy tails of the full-energy peaks are well

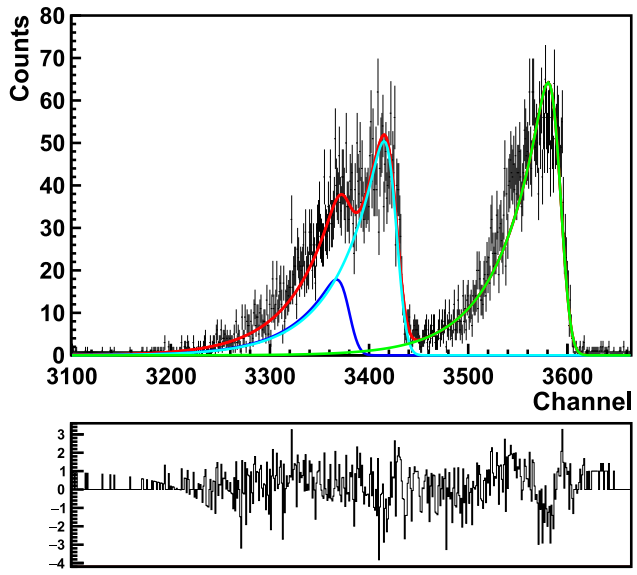

Fig. 5. Spectrum from the thorium source. The portion where the two lines from ^{228}Th (cyan and blue curves on the left) and the one from ^{224}Ra (green curve on the right) are located is singled out. The fit (red curve) has been performed with the RF from Eq. (3), as described in the text. The lower panel shows the ratio of the deviation from the fitted function to the statistical uncertainty for each bin.

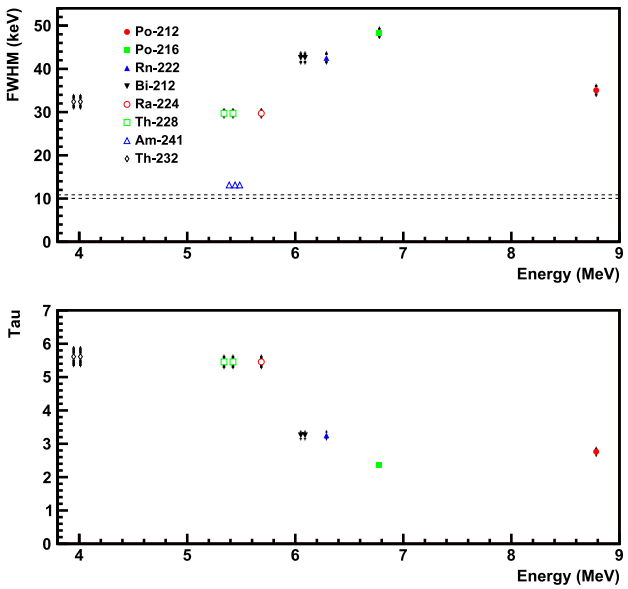

Fig. 6. Values of the parameters σ (converted to FWHM) and τ for the fits to the spectra used in the energy calibration (upper and lower panels, respectively). The error bars correspond to 1 standard deviation. The α-lines used are indicated in the legend of the upper panel. The horizontal dashed lines in the upper panel encompass the value obtained with a pulser with its statistical uncertainty (1 standard deviation). The lower panel contemplates the thorium decay sequence alone because a single value of τ is defined only for its fitting model, see Eq. (3).

preserved. The parameters σ, d_1, w_1, d_2, and w_2 are common to the three lines; moreover, only one overall normalization factor is free because the relative intensities have been fixed to the branching ratios tabulated by Bé et al. (2004). The values from the fit are $\tau_1 = 1.41 \pm 0.08$, $\tau_2 = 7.3 \pm 1.0$, $w_1 = 0.050 \pm 0.009$, and $w_2 = 0.38 \pm 0.02$. The Gaussian component in Eq. (5) is thus necessary since it accounts for the majority of the RF area.

A straightforward calibration could be carried out with the three lines from ^{241}Am visible in Fig. 4; unfortunately, the result would be too coarse to be of any use in the current context. We determined that a thorium source serves the purpose quite suitably because it delivers concurrently the lines from all the daughter isotopes in secular equilibrium. Namely, considering only the α emitting species: ^{232}Th, ^{228}Th,^{224}Ra, ^{220}Rn, ^{216}Po, ^{212}Bi, and ^{212}Po (in order of appearance along the decay chain). They populate the energy range from ≈8.8 MeV to ≈3.9 MeV and have all been included in the calibration for two main reasons. (i) The positions of the peaks from ^{241}Am are still covered, without any need for an extrapolation, even after crossing the targets. (ii) The span is comfortably large to allow an accurate determination of the slope of the calibration (which is the only parameter needed here). We found out that Eq. (3) is fully adequate to fit the spectra and recourse to Eq. (5) is not necessary. Moreover, two strongly overlapping α-lines are present in ^{232}Th,^{228}Th, and ^{212}Bi with sufficient yields to deserve being independently accounted for in the fits (their relative intensities have been fixed, again, to the branching ratios tabulated by Bé et al. (2004)). As an example, the two lines from ^{228}Th and the partially superimposed one from ^{224}Ra are shown in Fig. 5.

The overall consistency of the different fits must be inspected since they have been carried out separately. We discuss the two most important variables. The values of σ, converted to full-width at half maximum (FWHM), are plotted in the upper panel of Fig. 6. The error bars are those returned by the fit itself. It is important to mind that all the lines from the same isotope are adjusted with the same σ: namely, the three from^{241}Am, the two from ^{232}Th, the two from ^{228}Th and, finally, the two from ^{212}Bi. The pair of dashed horizontal lines, visible in Fig. 6, encompasses an interval of ±1 standard deviation around the resolution of 10.5 keV (FWHM) obtained with a pulser (which generates a Gaussian peak). Only the case of ^{241}Am at ≈13 keV (FWHM) comes close to the limit set by the electronic chain, actually somewhat below the declared expectation from the manufacturer (see Section 3.3). We attribute this difference to the thorium source not being as thin as the ^{241}Am one (see Section 3.2): some energy-loss straggling introduced additional broadening. This conclusion is in agreement with the mentioned observation that Eq. (5) is necessary for ^{241}Am, while Eq. (3) is fully adequate for the lines from the thorium decay sequence. Bortels and Collares (1987) linked, as well, the need to adopt a RF with an higher number of one-sided exponential components to the use of thinner sources.

The results for τ from the lines of the thorium decay sequence, ensuing from the same fits with Eq. (3), are reported in the lower panel of Fig. 6. The error bars have been attributed like in the upper panel. Here too, the constraint to have equal RF parameters was applied on the lines from the same isotopes. The values of τ are intermediate between those of τ_1 and τ_2 for ^{241}Am from Eq. (4) mentioned above (actually closer to τ_2 as implied by w_2 being ≈8 times w_1). The decrease of τ with energy is possibly linked to an improvement in charge collection (corresponding to faster dropping tails) for longer particle tracks (smaller chance of columnar recombination).

The reduced Pearson-χ^2 is plotted in the upper panel of Fig. 7, once more, for the same fits. It is important to pay attention that some groups of lines are adjusted together (because they partially superimpose, see e.g. Fig. 5) and only one global value of χ^2 is defined: namely, the three from ^{241}Am, the two from^{232}Th, the two from ^{228}Th along with the one from^{224}Ra, and, finally, the two from ^{212}Bi together with the one from ^{220}Rn. All values are reasonable, the worst case being that of ^{241}Am, despite the use of the more complete Eq. (5) instead of Eq. (3).

A linear fit to the position of all the 13 lines, as a function of the nominal energies tabulated by Bé et al. (2004), has, finally, been undertaken to obtain the channel to energy conversion factor. The slope of the calibration is (628.8 ± 0.3) channels/MeV. The reliability of the final outcome can be judged by inspecting the residuals displayed in the lower panel of Fig. 7. Two main comments are in order. Firstly, the points from ^{241}Am are indeed systematically above the others by a slight amount. It is possible that the energy losses, suffered inside the

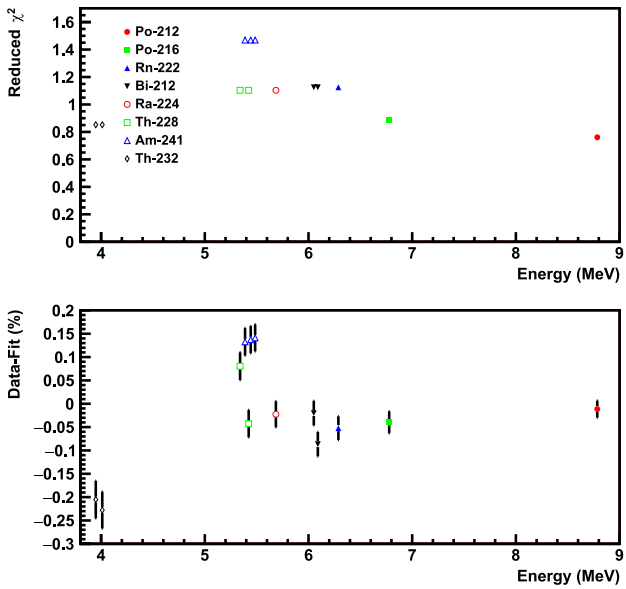

Fig. 7. Values of χ^2/ndf for the spectra used in the energy calibration (upper panel) and residuals from a linear energy to channel conversion (lower panel). The error bars in the lower panel correspond to 1 standard deviation. The α-lines used are indicated in the legend of the upper panel.

source, by all the lines from the thorium decay chain are systematically higher, as discussed above in connection with the consistently larger values of σ. However, such an effect is, at most, of ≈0.2%. Secondly, a linear calibration is working quite well: beyond the three ^{241}Am lines (affected by the first comment), the two others from ^{232}Th are too low by ≈0.2%. Note, however, that these are a pair of close ones and the fit may give inaccurate results, as it happens also in the case of ^{228}Th (see Fig. 7). Thus, attributing all the deviation by ≈0.2% to a non-linearity in the RF of the PIPS sensor is possibly an overestimation. We did not consider necessary to: (1) introduce a non-linear calibration; or (2) account, separately, for the energy lost in the entrance dead layer and for the nuclear energy loss in the active detector volume, as it was done by Moro et al. (2016) following a recommendation from Pascual-Izarra and Barradas (2008).

4.3. Determination of the energy lost in the targets

The spectra of the α-particles from the ^{241}Am source, transmitted through the Al, Cu, Sn, and Au targets, are plotted in Fig. 8. The most striking difference with respect to the direct one, see Fig. 4, is the spread introduced by energy straggling in the target: the three α-lines are not separable anymore and only one broad distribution is present.

It is possible to get a feeling about the general conditions to be met by the RF from Eq. (5) with a simple argument: the parameters d_1 and d_2 can be assumed to remain more or less unaltered being related to the intrinsic properties of the detector and to the energy of the α-particles. One can, then, anticipate that the value of τ_2 would drop to 1.2 and to even smaller values for the Cu and other targets, respectively (that of τ_1 would be about at least five times smaller). The influence of the asymmetric tail of the RF becomes, thus, small and an approximation with a single Gaussian is both adequate and necessary to ensure the convergence of the fit when the sensitivity to τ gets reduced (see also the comments made in Section 4.1). Any residual asymmetry visible in Fig. 8 is rather the consequence of the underlying three decay lines, which cannot be well separated. This last observation explains, as well, the root of another difficulty to be faced: the broadening described by the σ of the Gaussian (having only one common value for each target) is correlated with the separations

Table 3
Values of Pearson-χ^2/ndf for the fits to the spectra measured with the ^{241}Am source and the Al, Cu, Sn, and Au targets. The energy lost ΔE_1 by the α-particles from the most intense decay line of ^{241}Am (E_1 = (5.48556 ± 0.00012) MeV Bé et al., 2004), its statistical, estimated as 1 standard deviation, and systematic uncertainties are also given.

Target	χ^2/ndf	ΔE_1 MeV	Stat. unc. MeV	Syst. unc. MeV
Al	1.08	0.89449	0.00013	0.004
Cu	1.10	0.8816	0.0004	0.003
Sn	1.30	0.8074	0.0004	0.004
Au	1.25	1.2021	0.0006	0.006

between the lines and no convergence of the fit is possible if they are simultaneously left free. Therefore, both the relative intensities and the energy separation between the three lines have been fixed with the help of the tabulations published by Bé et al. (2004). Let us define, to streamline the exposition, $\Delta E_{12} = E_1 - E_2$ and $\Delta E_{13} = E_1 - E_3$ with $E_1 = (5.48556 \pm 0.00012)$ MeV the energy of the most intense peak (Bé et al., 2004) and $E_3 < E_2 < E_1$. A first fit has been carried out assuming the nominal $\Delta E_{12}^{(0)}$ and $\Delta E_{23}^{(0)}$ by Bé et al. (2004) (which are converted to $\Delta n_{12}^{(0)}$ and $\Delta n_{13}^{(0)}$ in channels using the gain from the calibration). This initial step gives a displacement in channels $\Delta n_1^{(0)}$ of the position of the line at E_1 with respect to the absence of target, which is converted into an estimate of the energy lost $\Delta E_1^{(0)}$ in the target itself (still using the gain from the calibration). We assume that the SCS $\mathcal{E}(E)$ in the target is well described by ASTAR, because indeed it will turn out to be the case (see Section 6), and integrate $1/\mathcal{E}(E)$ to convert $\Delta E_1^{(0)}$ into a mass thickness ρx_0. Once a first estimate of ρx_0 has been reached, it is possible to calculate, by integrating $\mathcal{E}(E)$, improved values of $\Delta E_{12}^{(1)}$ and $\Delta E_{13}^{(1)}$, which take into account the crossing through the target. The new $\Delta E_{12}^{(1)}$ and $\Delta E_{13}^{(1)}$ are converted back to $\Delta n_{12}^{(1)}$ and $\Delta n_{13}^{(1)}$ (once more using the gain from the calibration). A final fit is performed to determine a more accurate $\Delta n_1^{(1)}$ exploiting $\Delta n_{12}^{(1)}$ and $\Delta n_{13}^{(1)}$. The latter is, finally, used to arrive at our best estimate of $\Delta E_1^{(1)} = \Delta E_1$, see Table 3. The α-decay lines get approximately 10% closer after crossing the targets than they are without them (i. e. $\Delta E_{12}^{(1)} \approx 0.9\Delta E_{12}^{(0)}$ and $\Delta E_{13}^{(1)} \approx 0.9\Delta E_{13}^{(0)}$). Nevertheless, the effect on ΔE_1 is much smaller, remaining below 0.1% (i. e. $|\Delta E_1^{(1)} - \Delta E_1^{(0)}| \approx 0.1\%$) even in the worst case of Al: no further iteration of the procedure is needed. Care has been exercised to program all these operations in such a way that only the gain is used; thus, any uncertainty on the intercept of the calibration does not concern ΔE_1. The targets are not thin enough to assume that the SCS is constant along the α-particle path: accordingly, they are sliced up into many layers during the numerical evaluation of the above mentioned integrals. The values of the Pearson-χ^2 divided by the number of degrees of freedom ndf for the final fits are listed in Table 3 as well.

The statistical uncertainty on ΔE_1 is the outcome of the propagation of those on the positions of the most intense α-line at E_1 (without and with target) and on the gain from the calibration (see Section 4.2). All three are returned by the respective fits. The systematic uncertainties, also collected in Table 3, deserve a more detailed explanation provided in Section 4.5.

The values reported in Table 3 for the Al target have been treated in a somewhat different manner than for all the others. The Pearson-χ^2/ndf belongs to the fit of Fig. 8. However, 11 such spectra have been acquired to study the reproducibility with time and target position. They are used to estimate the contribution of these variables to the systematic uncertainties in Section 4.5. We do not have any reason to prefer any one of such measurements and, therefore, we supply in Table 3 their average weighted with their statistical uncertainties (Brandt, 2014). The corresponding statistical uncertainty quoted in Table 3 is, likewise, the standard uncertainty of the weighted average (Brandt, 2014).

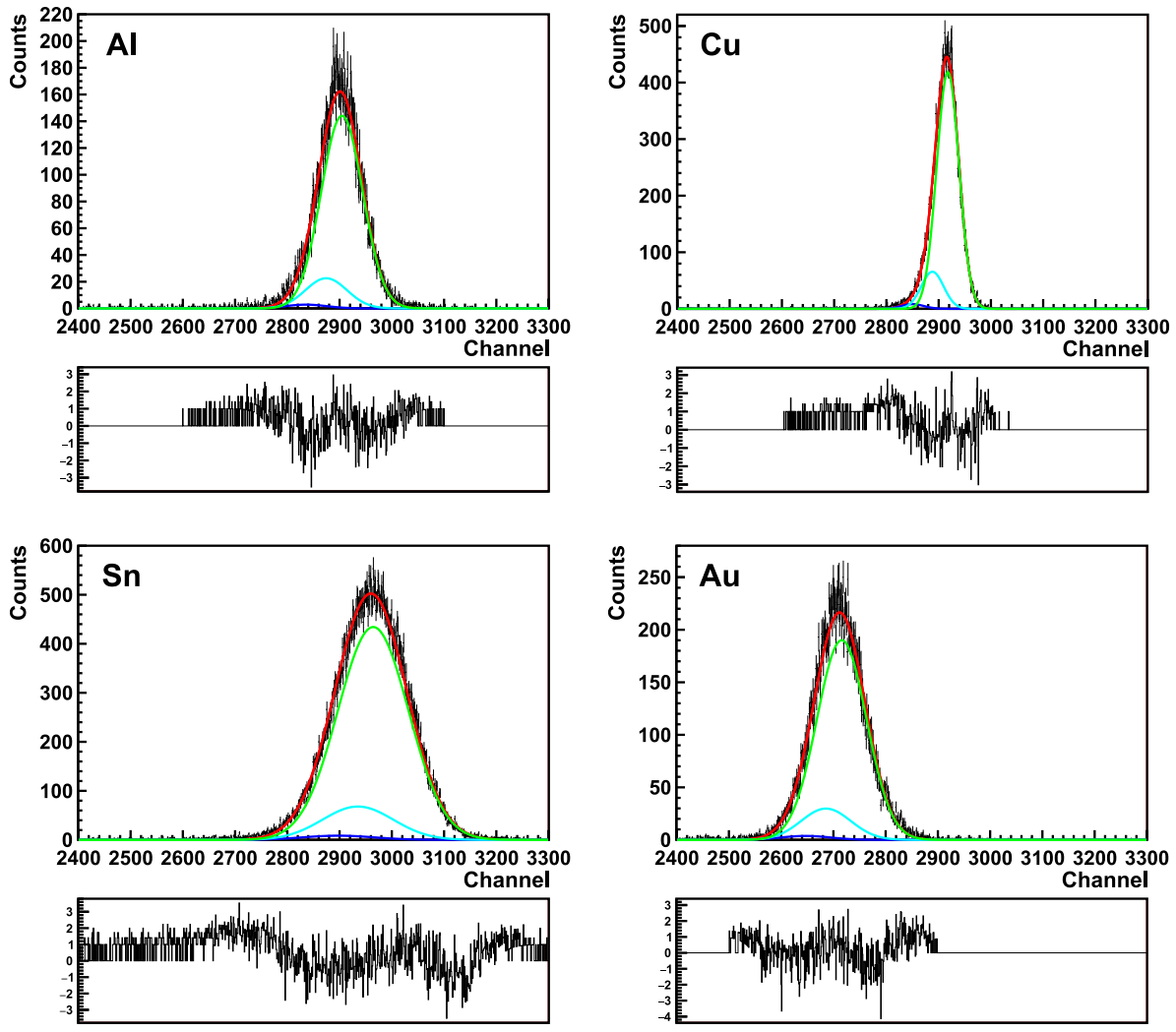

Fig. 8. Spectra measured with the ^{241}Am source and the Al, Cu, Sn, and Au targets. The fit (red curve) with the sum of three Gaussians, representing the three α-lines, is plotted together with each contribution (green, cyan, and blue curves). See the text for more details on how it is carried out. The lower parts show the ratio of the deviation from the adjusted function to the statistical uncertainty for each bin in the region where the fit has been performed.

Note that Table 3 already includes the correction for the average track length increase due to inclination ($\Delta\langle c_{tr}\rangle$ discussed in Section 4.4), for all targets, and that for the presence of impurities (explained in Section 4.5), for Al alone.

The σ of the Gaussian, one for each target, also contains interesting information. It is related to the spread of the histograms shown in Fig. 8, once due care is exercised for the presence of the three lines from ^{241}Am through the fitting model, as detailed above. The σ_0 of the Gaussian convolved with the RF model adopted for the direct spectrum of ^{241}Am (see Section 4.2) must also be subtracted quadratically to bring out the contribution from the target alone $\sigma_{\Delta E_1} = (\sigma^2 - \sigma_0^2)^{1/2}$. The final values are $\sigma_{\Delta E_1}$ = (62.9 ± 0.3), (33.5 ± 0.001), (107.6 ± 0.2), and (75.1 ± 0.2) keV for Al, Cu, Sn, and Au, respectively (the uncertainties are statistical only, representing 1 standard deviation). The corresponding ratios to the energy straggling calculated with the Bohr high-energy non-relativistic limit (Bohr, 1915, 1948) σ_B are $\sigma_{\Delta E_1}/\sigma_B$ = 3.0, 1.4, 4.2, and 2.1. The predictions for σ_{TRIM} from TRIM version 2013 (Ziegler et al., 2010) are close to σ_B so that $\sigma_{\Delta E_1}/\sigma_{TRIM} \approx \sigma_{\Delta E_1}/\sigma_B$ not explaining the measured discrepancies. The results for $\sigma_{\Delta E_1}/\sigma_B$ are an indication of the presence of microscopic (sub-millimeter) inhomogeneities of the foils: Sn being the worst one, in agreement with a larger observed number of holes (see Section 3.1), while Cu is the best. By the way, we searched for α-particles passing through the holes and, thus, appearing with the full energy in the Sn and Au spectra, finding nothing statistically relevant above the expected background. The probability for a decay happening in the region of the surface belonging to the ^{241}Am source just below the hole and producing an α-particle in the direction of the hole itself is too small to be observed. It is also important to remark that such small-scale fluctuations in the thickness average out over the aperture of the collimators (6 mm in diameter, see Section 3.3) and do not affect ΔE_1 (related to the first moment of the histograms displayed in Fig. 8). The situation is different for the large-scale (millimetre) variations that contribute to the systematic uncertainty in ΔE_1 (see Section 4.5). The typical size of the former is more than one order of magnitude bigger than that of the latter (compare $\sigma_{\Delta E_1}/\Delta E_1$ with the 2nd column of Table 4).

4.4. Track-length correction

The α-particles do not always hit the target perpendicularly. In general, their tracks form an angle θ with the normal to the surface of the source. An estimate of the largest inclination, θ_{max}, can directly be made from Fig. 3 by considering a line that grazes the borders of the lower and upper collimator holes on opposite sides: it is $\theta_{max} \approx 7.2°$. The track length inside the target, c_{tr}, can, correspondingly, suffer an extension of $\Delta c_{tr} \approx 1\%$ in the worst scenario. The measured lost energy is proportionally increased undergoing a change larger than

the statistical uncertainties compiled in Table 3 or the systematic ones discussed in Section 4.5 and must, therefore, be better studied.

A simple Monte Carlo program has been written in `Fortran` to simulate decays uniformly spread over the source (assumed to be a disc with a diameter of 7 mm, see Section 3.3) and emitting isotropically into the forward hemisphere. The α-particles are, afterwards, propagated along a straight line checking if they pass the collimation system and if they finally reach the active surface of the detector. Approximately 43% and 3.0% of the forward-moving α-particles go through the entrance and exit holes, respectively, with the dimensions given in Fig. 3. The same 3.0% hits the PIPS sensor without additional reductions. The average relative increase of the target thickness is $\Delta\langle c_{\mathrm{tr}}\rangle = (0.10577 \pm 0.00002 \pm 0.00005)\%$ for this particular subclass of tracks connecting the source and the detector. The first and second uncertainties are statistical and systematic, respectively. The latter has been estimated by using a larger source disk radius of 8 mm. It is the least known parameter of the geometry and it furnishes a somewhat exaggerated upper limit.

The result found for $\Delta\langle c_{\mathrm{tr}}\rangle$ indicates that the simple argument presented at the beginning of this Section is a large overestimate disregarding the portion of the source disk visible under each inclination θ. The correction $\langle c_{\mathrm{tr}}\rangle$ has already been applied in Table 3; but the corresponding uncertainties are not taken into account due to their smallness when compared to the others, see Section 4.5.

4.5. Budget of the systematic uncertainties

The systematic uncertainties need to be discussed separately for the two fundamental quantities relevant in the current work: the mass thicknesses of the targets, ρx_0, (see Table 2) and the energies lost in them by the α-particles, ΔE_1 (see Table 3).

The systematic effects on $\rho x_0 = \Delta m/\Delta A$ originate from the determination of the area ΔA and of the mass Δm, see Section 3.1. The largest difficulty in settling the surface of the foil ΔA is its delimitation on the scanned image due to the irregularities of the borders. A manual procedure has been actually found to be superior to the automatic one implemented in the ImageJ code. The associated fluctuations are already accounted for by the standard deviation listed in Table 2 because the ten images have been taken with different orientations (see Section 3.1) repeating the manual identification of the edges. However, the calibration of the scanner with the ruler is not free of problems. A portion of approximately 50.0 mm with finer marks every 0.5 mm has actually been employed with an accuracy essentially arising from their width. We estimate it as being 0.05 mm or 0.1% for each dimension. The final impact on the thickness can be found in Table 2.

Five possible sources of biases on Δm can disturb the weighing process, according to the manufacturer of the microanalytical scale (Reichmuth, 2001): (i) readability, (ii) repeatability, (iii) corner load deviation, (iv) non-linearity, and (v) sensitivity drifts due to temperature and time. The first three are actually included in the statistical uncertainty given in Table 2 due to the way the measurements have been repeated (see Section 3.1). Mettler Toledo® grants a maximum non-linearity deviation of 4 μg for the XP6. It is, possibly, a large overestimation of the systematic error because it does not necessarily apply to the masses being measured. The thermal and time sensitivity drifts declared for the XP6 are 0.0001% per degree and per year, respectively. They are not expected to play a major role. We have been able to confirm such a conclusion by weighting the Al foil with two other different scales (also manufactured by Mettler Toledo®, models MX5 and UMX2) installed at the Laboratório de Anlálise de Processos Atmosféricos (LAPAt) of the Institute of Astronomy and Geophysics of the University of São Paulo (IAG-USP, Brazil) with similar cares to those described for the LFA (see Section 3.1). The maximum deviation found has been 0.0016%, which we regard as a reasonable estimate of the residual systematic error on the mass determination deriving from items (iv) and (v). It can safely be ignored, being much smaller than that on the area.

Table 4
Contributions to the systematic uncertainties in the determination of the energy ΔE_1 lost in the four targets.

Target	Time stab.	Uniformity	Impurities	Total
Al	0.33%	0.05%	0.04%	0.42%
Cu	0.33%	0.05%	0.001%	0.38%
Sn	0.33%	0.05%	0.10%	0.48%
Au	0.33%	0.13%	0.07%	0.53%

The measurement of the lost energy ΔE_1 is subject to three main sources of systematic uncertainties: (i) time drift of the energy calibration between the relatively long measurements (days), (ii) large-scale (millimetre size) target non-uniformities over dimensions comparable to those of the collimator holes, and (iii) impurities present in the foils.

A series of 11 acquisitions has been repeated with the Al target over a period of approximately one month. The deviations in the reconstructed ΔE_1 over the full time span of the runs have been used to quantify the impact of (i). The maximum discrepancy found has been 0.33% (see Table 4).

The setup allows to displace the target to the left and to the right, with respect to the nominal position, by 1 mm. Larger shifts are not warrant if the exit hole of the collimator has to remain completely covered by the foil. They have been repeated separately for the Al, Cu, Sn, and Au targets to gauge item (ii) above. Two acquisitions with the target in the nominal position have been made before and after the dislocations to monitor the time stability. The estimated non-uniformities are collected in Table 4. The observed variations for Al, Cu, and Sn are below the sensitivity of the procedure given by the drift between the first and last spectra in the nominal position. Therefore, to be conservative, the latter is entered into Table 4. The non-uniformity of an Al target made from the same roll (see Section 3.1) was found to be 0.46% by Moro et al. (2016), employing the LAMFI proton beam with energies between 0.9 and 3.6 MeV and a size of ≈2 mm, much smaller than that of the holes of our collimator (see Section 3.3). It is, thus, generally consistent that a larger averaging area gives a smaller value.

The effect of the impurities (contribution (iii) above) has been studied with ASTAR, anticipating the conclusion of Section 6. The additivity rule by Bragg and Kleeman (1904) has been assumed, which is a good approximation for metallic films and the atomic numbers involved. The measured area ΔA and mass Δm, see Section 3.1, directly fix the mass thickness of each target $\rho x_0 = \Delta A/\Delta m$, independently from the presence of contaminants, so that the appropriate quantity to be studied is the variation in the mass stopping power S/ρ and not in the SCS $\mathcal{E}$. The case of the Al target must be specifically handled because direct information on the type and abundance of the trace elements is available from the RBS analysis made on another item fabricated from the same roll by Moro et al. (2016), as recalled above. The cumulative effect of all of them is to increase the measured ΔE_1 by $(0.14 \pm 0.04)\%$, where the error has been assessed conservatively considering the discrepancy between the ASTAR and SRIM 2013 predictions. The most unfavourable combination of the uncertainty intervals attributed to C, O, Fe, Mn, and Zn by Moro et al. (2016) (see Section 3.1) yield a lower estimate of 0.02%. We have adjusted the measured ΔE_1 given in Table 3, as it was also done by Moro et al. (2016). Accordingly, the sole error on such a correction has to enter into Table 4. No RBS has been made for the Cu, Sn, and Au foils. Only the results of typical analyses, as stated by Goodfellow, are available. The ensuing percentage change of ΔE_1 is reported in Table 4. We did not alter ΔE_1 since the actual composition of our targets may differ somewhat from the average case and left all the effect as a cautious estimate of the systematic uncertainty associated to impurities.

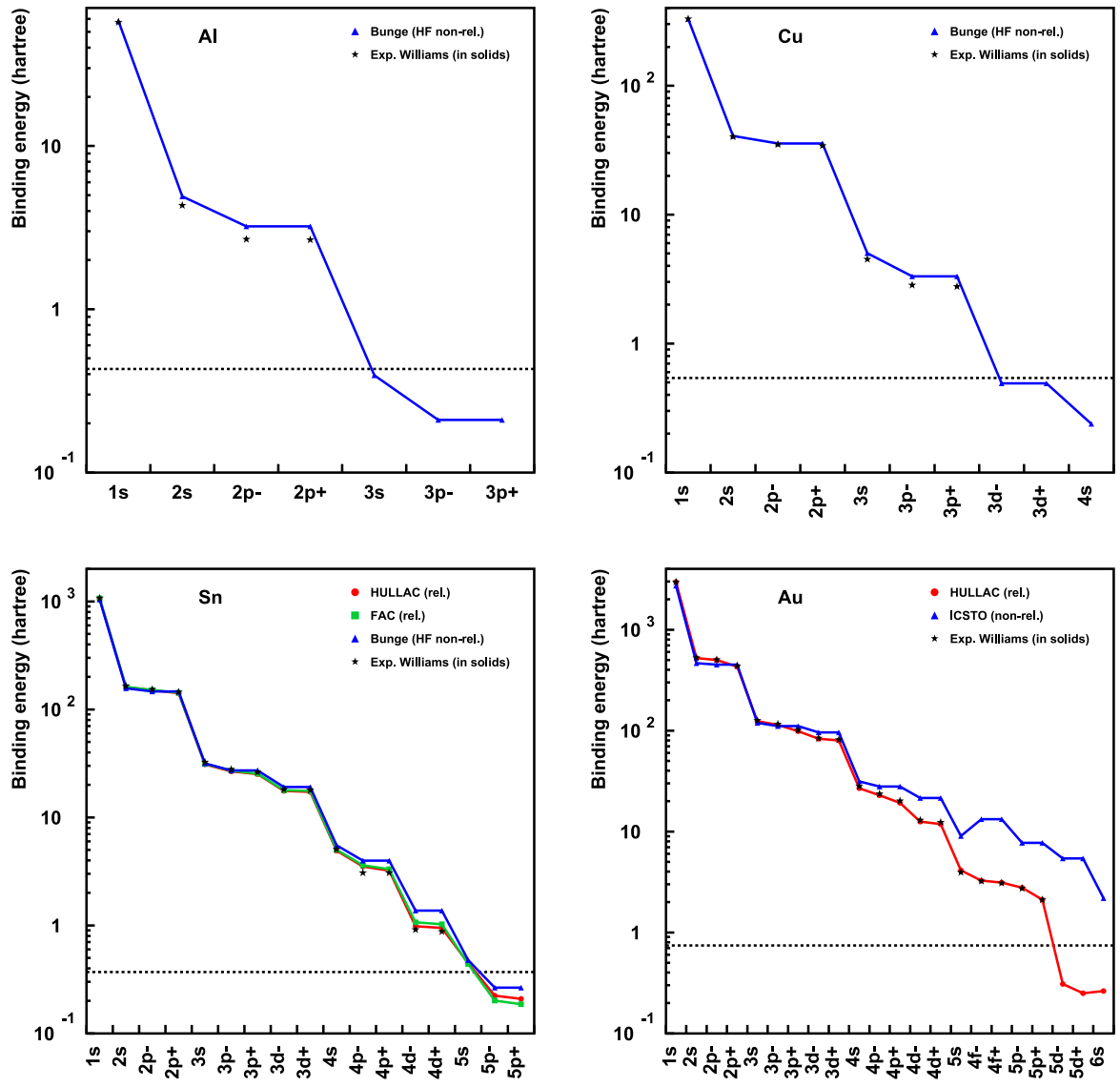

Fig. 9. Theoretical binding energies of the occupied (sub)shells for Al, Cu, Sn, and Au. The relativistic predictions ensuing from the HULLAC package by Bar-Shalom et al. (2001) are shown for Sn and Au (red circles and curve). Moreover, the relativistic FAC code by Gu (2008) has also been considered for Sn (green squares and curve). The values by Bunge et al. (1993), obtained within a non-relativistic Hartree–Fock approach, are plotted for Al, Cu, and Sn (blue triangles and curve). The non-relativistic ICSTO package by Badnell (2011) has been run for Au (blue triangles and curve). The experimental binding energies in solids by Williams (2015) are plotted for comparison (black stars). Dotted horizontal lines correspond to the Fermi energy of the DEG, E_F.

5. First-principles calculation

The measurements offered in the present work represent a good tool to probe first-principles calculations. The shellwise local plasma approximation (SLPA-LM) by Montanari and Miraglia (2013), as improved by Peralta et al. (2022, 2023), has been selected to predict theoretical SCSs of α-particles in metals. This model describes the electronic stopping considering the contributions of each atomic (sub)shell within the quantum dielectric formalism. It employs the Levine–Mermin (see below) ε^{LM} and the Mermin (1970) ε^{M} dielectric response functions for the bound and the valence or conduction electrons (Peralta et al., 2022, 2023) of the metal, respectively.

5.1. General considerations and inputs

The SLPA describes the inelastic response of the target electrons to the ion perturbation (ionisation, energy loss, and energy-loss straggling). It considers the electrons of similar binding energies as one single electron cloud, characterized by their local density around the target nucleus, that responds collectively to the external action, including binary collisions (single-electron and electron–hole pair) as well as collective excitations, screening among electrons, and electron–electron correlations in the final state. Furthermore, it assumes the independent response of electrons with different binding energies. The model relies on the electronic structure of the target, namely the theoretical (sub)shell wave functions and the corresponding binding energies, supplemented by a damping constant.

The metals investigated here differ significantly, with their atomic numbers ranging from 13 to 79. We employ two theoretical approaches to describe their electronic structure. We rely on the non-relativistic Hartree–Fock results by Bunge et al. (1993) for Al and Cu. On the other hand, in the case of Sn and Au, we solve the many-electron Dirac Hamiltonian using the perturbative parametric potential model included in the HULLAC package by Bar-Shalom et al. (2001) and the self-consistent method with an effective potential implemented in the FAC code by Gu (2008).

The theoretical binding energies for the (sub)shells of Al, Cu, Sn, and Au are displayed in Fig. 9. The importance of performing relativistic calculations, with the above mentioned HULLAC and FAC packages, is assessed by confronting the predicted binding energies with the non-relativistic ones. The latter were taken from the work by Bunge et al. (1993) (based on Roothaan–Hartree–Fock wave functions) and from calculations with Autostructure by Badnell (2011) (based on Intermediate Coupling Slater Type Orbitals (ICSTO)) for Sn and Au, respectively. Although the differences between the non-relativistic and relativistic results are visible for all (sub)shells, the discrepancies are larger for the outer ones. A comparison with experimental values for solid targets (Williams, 2015) is displayed as well in Fig. 9. It is worth stating explicitly that the aforementioned atomic-structure calculations pertain to isolated atoms. No experimental binding energy is available for the electrons belonging to the conduction band, or the degenerate electron gas (DEG), of metals, as expected. The corresponding Fermi energy, E_F, is highlighted by the horizontal lines introduced in Fig. 9. The improvement brought about by the relativistic treatment is evident, in the case of Sn and Au, for the N and higher subshells. More details about the relativistic calculations and the results for Zr, Nb, Pd, Er, Gd, Hf, Ta, Os, and Pt were given by Mendez et al. (2019).

5.2. SLPA-LM calculation

The SLPA-LM approximation implies that the dielectric formalism is applied to all atomic electrons. The SCS for a bare ion with charge Z_1 moving with velocity v is obtained by adding the independent contributions

$$\mathcal{N}\,\mathcal{E}_i = \frac{2Z_1^2}{\pi v^2}\int_0^\infty \frac{dk}{k}\int_0^{kv}\omega\,\mathrm{Im}\left[\frac{-1}{\epsilon_i(k,\omega)}\right]d\omega\ , \tag{6}$$

where the subindex i refers to a bound atomic (sub)shell or the DEG that models the valence electrons. The energy-loss function of each bound (sub)shell is expressed as

$$\mathrm{Im}\left[\frac{-1}{\epsilon_i(k,\omega)}\right] = \mathcal{N}\int \mathrm{Im}\left[\frac{-1}{\epsilon^{\mathrm{LM}}\left(k,\omega;\rho_i(r),E_i,\gamma_i(r)\right)}\right]d^3\mathbf{r}\ . \tag{7}$$

The dielectric response function ϵ^{LM} corresponds to the Levine–Mermin (Mermin, 1970; Levine and Louie, 1982) (LM) formulation by Peralta et al. (2022), which explicitly includes the binding energies E_i and local electron densities $\rho_i(r)$ of the ith (sub)shell as well as a phenomenological local damping $\gamma_i(r) = \sqrt{\pi\rho_i(r)}$. In turn, the contribution of the DEG to the SCS takes the form of Eq. (6) with the energy-loss function $\mathrm{Im}\left[-1/\epsilon^{\mathrm{M}}(k,\omega)\right]$, whose parameters are the Fermi energy (or the one-electron radius r_s) and the damping constant of the DEG, see below.

The theoretical number of electrons in the valence shell, necessary for applying Eq. (6), is clear for Al ([Ne] $3s^2\ 3p^1$) and Sn ([Kr] $4d^{10}\ 5s^2\ 5p^2$), namely $N_e^{\mathrm{Al}} = 3$ ($r_s = 2.07$, $E_F = 0.428$ in atomic units) and $N_e^{\mathrm{Sn}} = 4$ ($r_s = 2.22$, $E_F = 0.373$). The distinction is less sharp for transition metals, i. e. Cu ([Ar] $3d^{10}\ 4s^1$) and Au ([Xe] $5d^{10}\ 6s^1$): some d electrons are promoted to the DEG while others remain bound. We decided to take $N_e^{\mathrm{Cu}} = 3$ ($r_s = 1.85$, $E_F = 0.537$), and $N_e^{\mathrm{Au}} = 7$ ($r_s = 1.57$, $E_F = 0.742$), after examining the experimental optical energy-loss functions compiled by Werner et al. (2009). The damping constant of the DEG is also inferred from the work by Werner et al. (2009), namely $\gamma = 0.037$, 0.29, 0.046, and 0.12 for Al, Cu, Sn, and Au, respectively. The value chosen for Sn is actually that of Te because Werner et al. did not report the optical energy-loss function of the former. The number of electrons assigned to the DEG is a crucial parameter for calculations at energies around and below the maximum of the SCS. However, in the energy interval analysed here, the overall SCS is nearly independent from the number of electrons in the DEG and first sub-valence shell, as long as their total amount stays correct.

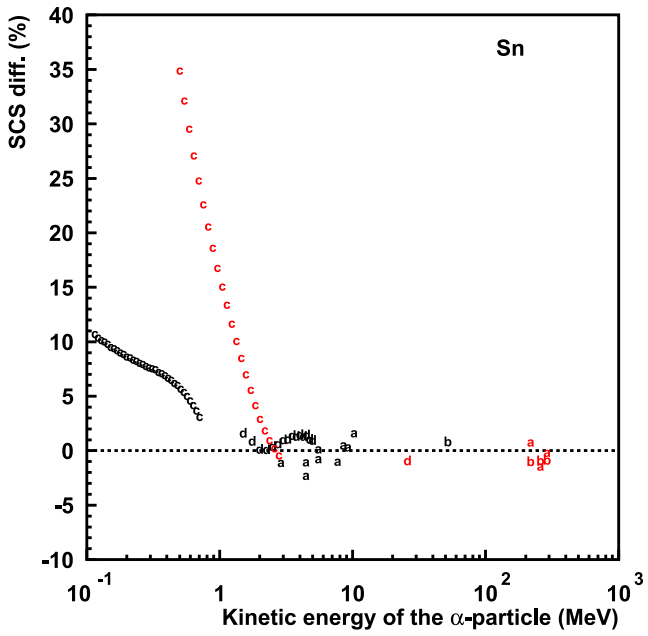

Fig. 10. Experimental SCSs of Sn for He-ions and protons from the IAEA database (Montanari and Dimitriou, 2017; Montanari et al., 2024; Montanari, 2025) after 1990 (included). The smooth behaviour, predicted by the ICRU Report 49 (Berger et al., 1993) for He-ions, has been subtracted from the SCSs (black letter keys, see Table 1) to ease the visualization, as in Fig. 1. The proton SCSs have been scaled with Z_1^2 at the same velocity (red letter keys: a Sakamoto et al. (1991), b Bichsel and Hiraoka (1992), c Eppacher and Semrad (1992), and d Shiomi-Tsuda et al. (1994)).

5.3. The equilibrium charge state of He ions in Al, Cu, Sn, and Au

The dielectric formalism assumes a linear response because it is based on first-order perturbation theory. Correspondingly, a dependence with the square of the ion charge Z_1 appears in Eq. (6). However, Z_1 need not be that of the bare α-particle. The He ion interacts with the electrons of the atoms in the traversed medium, which gives rise to a sequence of capture and ionisation processes. The multiple electron transfers inside the solid make the projectile reach an equilibrium charge state that depends on its velocity. The electronic capture becomes negligible, at high ones, and the equilibrium charge state tends to be +2. We estimated the energy range where the charge state is +2 by assessing the validity of the Z_1^2-scaling (for the same velocity). A comparison of the experimental SCSs for H and He ions crossing the materials of our targets has been carried out exploiting, once more, the IAEA database (Montanari and Dimitriou, 2017; Montanari et al., 2024; Montanari, 2025). The case of Sn is displayed, as an example, in Fig. 10. The common behaviour, expected for He-ions according to the ICRU Report 49 (Berger et al., 1993) (ASTAR), has been subtracted to render deviations easily identifiable, as in Fig. 1. We have, thus, verified that the charge state of He is +2 for impact energies above ≈1.2, ≈2.0, ≈2.0, and ≈1.6 MeV for Al, Cu, Sn, and Au, respectively. Thus, in the energy range of present concern, we calculated the SCSs for He^{2+} ions assuming the Z_1^2-scaling. Stronger arguments can be made for Al and Au, see Section 6. They reach much better accuracies than those of the available data (see Figs. 1 and 10).

6. Results and discussion

The Al, Cu, Sn, and Au targets of the current work are not thin enough to warrant the assumption that the energy loss or, equivalently, the SCS, is constant along the path of the α-particles inside them. It is hardly possible to avoid such a limitation if a direct measurement of the mass thickness, $\rho x_0 = \Delta m/\Delta A$, by the mass, Δm, and the area,

Table 5
Comparison of the measured energy ΔE_1 lost in the Al, Cu, Sn, and Au targets, see Table 3, with the theoretical expectations from ASTAR, SRIM version 2013, `cbethe`, and the SLPA-LM approach. The quoted statistical and systematic uncertainties on the data are a quadratic and linear sums, respectively, of the contributions from ΔE_1 itself, see Table 3, and the target thickness, see Table 2. The signs of the differences between measurements and calculations are given assuming the former as reference.

Target	Exp			ASTAR		SRIM		`cbethe`		SLPA-LM	
	ΔE_1 MeV	stat. %	syst. %	ΔE_1 MeV	diff. %	ΔE_1 MeV	diff. %	ΔE_1 MeV	diff. %	MeV	%
Al	0.8945	0.05	0.6	0.8935	−0.1	0.8909	−0.4	0.8738	−2.3	0.8533	−4.6
Cu	0.8816	0.09	0.6	0.8790	−0.3	0.8643	−2.0	0.8427	−4.4	0.9152	3.8
Sn	0.8074	0.14	0.7	0.8088	0.2	0.8075	0.0	0.7790	−3.5	0.7937	−1.7
Au	1.2021	0.11	0.7	1.2038	0.1	1.2156	1.1	1.1655	−3.0	1.2872	7.1

ΔA, is desired. Thus, the theoretical prediction for the lost energy, ΔE_1, must be determined by the condition that ρx_0 equals the mass range difference ρx in the continuous-slowing-down approximation

$$\rho x(E_\mathrm{i} \to E_\mathrm{f}) = \frac{\mathcal{M}}{N_\mathrm{A}} \int_{E_\mathrm{f}}^{E_\mathrm{i}} \frac{dE}{\mathcal{E}(E)} \tag{8}$$

where $\mathcal{M}$, N_A, and $\mathcal{E}(E)$ are the molar mass of the target species, the Avogadro constant, and the SCS for an α-particle with kinetic energy E in the considered material, respectively. The kinetic energies of the α-particles entering and exiting the target are E_i and E_f, respectively, so that $\Delta E_1 = E_\mathrm{i} - E_\mathrm{f}$. The integral in Eq. (8) is evaluated with a Gaussian adaptive quadrature from Quadpack by Piessens et al. (1983) and the condition $\rho x(E_\mathrm{i} \to E_\mathrm{f} = E_\mathrm{i} - \Delta E_1) = \rho x_0$ sought iteratively with the Brent method (Press et al., 1992). The expectations for the SCSs from ASTAR, SRIM version 2013, `cbethe`, and the SLPA-LM approach are confronted with the data from Section 4.3 in Table 5. The statistical and systematic uncertainties on the experimental ΔE_1 arise from the combination with quadratic and linear sums, respectively, of the corresponding relative contributions on ρx_0 and ΔE_1 from Tables 2 and 3, respectively. In fact, ρx_0 enters into the theoretical calculation through the constraint $\rho x(E_\mathrm{i} \to E_\mathrm{f} = E_\mathrm{i} - \Delta E_1) = \rho x_0$ enforced upon Eq. (8). The relative accuracy in the Gaussian quadrature has been set to 10^{-6}. The original `Fortran` code supplied by NIST is exploited to calculate the SCSs from ASTAR at an arbitrary energy. It internally implements a spline interpolation of the tables from the ICRU Report 49 (Berger et al., 1993). The energy grid for the output of the SRIM program cannot be easily changed: a linear interpolation on a log–log scale has been carried out on the default one. The differences in ΔE_1, when a spline (Press et al., 1992) is chosen instead, are at most of 0.02% for all the four targets. The default sampling of `cbethe` has a step size of 25 keV while the SLPA-LM calculations have been run on a mesh of 150 equally-spaced points between 4.0 and 5.5 MeV. A spline interpolation has been relied upon in both cases.

The Al target employed by Moro et al. (2016) and the present one were both fabricated from portions of the same roll, as mentioned in Section 4.4. The former was used to obtain SCSs for protons between 0.9 and 3.6 MeV. Moro et al. (2016) fitted the parameters of the original expression by Varelas and Biersack (1970) (see their Eq. (7)) to the available proton data between 0.5 and 4.0 MeV (i.e. by Moro et al. (2016) and from all previous publications listed in the IAEA database at that time). The numerical values are given towards the end of the right column on page 9 of the publication by Moro et al. (2016). We have evaluated numerically Eq. (8) with $\mathcal{E}$ from the Varelas–Biersack expression, with the parameters by Moro et al. (2016), taking, of course, the due provision for the Z_1^2-scaling and for the kinetic energy correspondence between protons and α-particles with the same velocity. The match to the ΔE_1 from Table 5 is within 0.5%. Such an agreement, beyond lending support to the estimates of the systematic uncertainties quoted in Table 5, confirms as well that the charge state of the He-ions (at least in Al) is indeed $Z_1 = +2$.

Let us now turn to a discussion of the comparison with theory. The semi-empirical ASTAR model behaves extremely well with a maximum deviation from the data for Cu of −0.3%, which is half the anticipated systematic uncertainty. It is based on the Bethe–Bloch formula with the Bloch, Barkas–Andersen, shell, and density-effect corrections, as mentioned, above a kinetic energy threshold, T_2, of 4.0, 6.0, 5.0, and 2.0 MeV for Al, Cu, Sn, and Au, respectively (see Table 3.7 by Berger et al. (1993)), where the He-ions can be assumed to have a charge state of $Z_1 = +2$. The merge with a fully empirical expression fitted to measurements, employed below an energy cut-off, T_1, of 1.0, 2.0, 2.0, and 1.0 MeV, respectively, was made with a spline by Berger et al. (1993). The present experiment reaches down to $E < T_2$, towards the end of path inside the target, for Cu and Sn, where, apparently, discrepancies are larger. The ASTAR shell corrections for Al, Cu, and Sn are the same as those of the ICRU Report 37 (Berger et al., 1984) for electrons (ESTAR). It is called Model 1 by Berger et al. (1993). A new Model 2 was introduced for seven high-Z elements including Au by Berger et al. (1993). The former approximated the atomic wave functions of the K and L shells with hydrogenic ones, while the latter extended the same procedure to the M ones as well. The remaining electrons (if any) are described with empirical modifications of the expressions for the L or M shells depending on whether Model 1 or 2 is being applied. Model 1 and 2 work very well for Al and Au, respectively, judging from Table 5. Their parameters (as well as the mean excitation energy I) were adjusted to selected proton data (Berger et al., 1984, 1993), so that the present study furnishes an independent validation with α-particles. Moreover, it also confirms that $Z_1 = +2$ with high accuracy, at least for Al and Au, where the kinetic energy after leaving the foil is still above T_2.

The general philosophy behind SRIM is quite similar to ASTAR. However, SRIM (for all versions released after 1985) is distributed only as a Windows® executable, preventing full knowledge of its physical content. It is included here due to its wide popularity in many areas of applied physics, mostly because it covers all pure elements (ASTAR accounts for about half of them) and many common compounds, as targets, beyond all ionic species, as projectiles. The 1985 source code was fully documented in the book by Ziegler et al. (1985). The SCSs for α-particles were based on those of protons with a description of the equilibrium charge state. This was apparently still the case in the 1995 version (Ziegler, 2004). However, the handling of the protons was altered between 1985 and 1995. An empirical parameterisation of the type introduced by Varelas and Biersack (1970) was adjusted to data in the former. A Bethe–Bloch-like expression with Bloch, Barkas–Andersen, shell, and density-effect corrections was preferred above 10.0 MeV in the latter. If this remained true in the 2013 version (undocumented), the present experiment probed the empirical part. Beyond the expressions adopted in ASTAR and SRIM, the set of measurements fitted to extract the needed parameters are certainly different. It seems that the choices made by the authors of SRIM are worse than those by the ones of ASTAR, except for Sn (where, remarkably, fewer publications were released, see Table 1).

A recent attempt by Salvat et al. (2022) and Salvat (2022) to improve the shell correction in the semi-empirical methods relying on the Bethe–Bloch formula has also been analysed. Its main advantage is to profit from much more realistic Dirac–Hartree–Fock–Slater wave functions for all (sub)shells. The energy ranges relevant for our data,

unfortunately, reach below the validity limit of 5.0 MeV stated for α-particles by Salvat (2022). Salvat (2022), however, sets the same threshold for protons to 0.75 MeV, corresponding to 3.0 MeV for α-particles, which covers the needs of the present work. We interpret the discrepancy as arising from concerns about the possible equilibrium charge state. We are rather sure that for Al and Au the issue is not relevant, as explained above, and attempted to apply the SCSs for protons by Salvat et al. (2022) and Salvat (2022) with the appropriate scaling for $Z_1 = +2$ and the projectile velocity.[5] The discrepancies ended up to be −2.3% and −3.0% for Al and Au, respectively, see Table 5.

The SLPA-LM values displayed in Table 5 agree to the measurements within few percent, except for the Au target, where the mismatch reaches up to 7%. This is within the expectations for such a model. The SLPA-LM approach adds contributions from the conduction band and the bound (sub)shells, with the theoretical atomic wave functions and binding energies being the main inputs for the latter, as mentioned in Section 5. Different factors limit the precision of a model, depending on the approximations introduced. One can highlight the following aspects for the SLPA-LM one: the number of subshells explicitly accounted for (including the 4f-shell of Au), the calculated binding energies (the disagreement between theory and experiment for the 2p-shell of Al is around 20%, see Fig. 9), and the uncertainty on the number of d-electrons promoted to the conduction band (this affects the Cu and Au results, although, in the energy range of the present data, it should be negligible, see Section 5), beyond the approximations intrinsic to the dielectric formalism itself or the proposed phenomenological local damping for the response of the bound electrons. We checked the possible impact of the uncertainties on the input parameters by computing again ΔE_1 for the Al target with the experimental binding energies. The −4.6% of Table 1 gets reduced to −3.0%. On the other hand, the results for Sn, with a difference of less than 2% from the measured values, are promising because it is the first time the energy loss is calculated by the SLPA-LM method for such a material. Thus, no compelling reason appears, at the moment, to question its basic assumptions.

7. Conclusion

The α-particles from ^{241}Am have been made to cross metallic foils of Al, Cu, Sn, and Au. The energy lost, ΔE_1, by those corresponding to the most intense line ($E_1 = (5.48556 \pm 0.00012)$ MeV) has been measured with a solid state detector. The gain calibration has been carried out with the ^{241}Am source and a natural thorium deposition, covering the energy range from ≈8.8 MeV to ≈3.9 MeV. They are both thin to avoid as much as possible any additional contribution to ΔE_1 (one important aspect of the present work). The mass thickness $\rho x_0 = \Delta m/\Delta A$ of the targets has been directly determined by finding out their mass Δm and surface area ΔA. This avoids any reference to the stopping powers of other particle species. Unfortunately, the films must endure the procedure and cannot be as thin as needed to yield a SCS.

The final impact of the statistical errors is negligible, being around 0.1%. The measurements are rather limited by the systematic uncertainties estimated to be 0.6 to 0.7%, combining those on ΔE_1 itself and on ρx_0 (since both enter when a comparison with theory is attempted). The largest part of 0.33% ensues from the long-term stability of the electronics. The non-uniformities of the films and their impurities have smaller influences. The aperture of the collimator of the α-particles is 6.5 mm, much wider than typical accelerators beams. This helps to explain why small-scale (sub-millimeter) point-to-point variations in the thickness of the targets were smeared out on ΔE_1. The average track inclination increased ΔE_1 by ≈0.1% and has been corrected for.

A comparison to the tables from the ICRU Report 49 (Berger et al., 1993) (ASTAR) has revealed an excellent agreement for all the materials covered by the present experiment, the worst difference on ΔE_1 being −0.3% for Cu. The SRIM program (version 2013) has a less uniform overall performance: it works better than ASTAR for Sn, behaves similarly for Al, but reaches discrepancies of 1.1% to −2.0% for ΔE_1 in Au and Cu (the normalization target of Mangiarotti et al. (2021b)), respectively. Both ASTAR and SRIM are based on semi-empirical approaches, where the needed parameters have to be extracted from stopping power measurements themselves on a material-by-material basis. We attribute the worse reliability of the latter to their choice. Shell corrections from realistic Dirac–Hartree–Fock–Slater wave functions end up deteriorating the quality of the agreement up to 4.4%.

The shellwise local plasma approximation (SLPA-LM) represents a modern first-principles calculation exploiting exclusively the theoretical (sub)shell wave functions and binding energies, supplemented by a damping constant. It makes, at variance of both ASTAR and SRIM, no use of the experimental stopping powers themselves. The mismatch with the present measurements is at most of a few percent for Cu and Sn. The ΔE_1 for the latter (never calculated with such an approach in the published literature) is predicted with an accuracy of −1.7%. The situation is less favourable for Al (−4.6%) and Au (7%). The quality of the input parameters (most notably the binding energies for Al and the complex shell structure of Au) are currently limiting the precision of the model.

CRediT authorship contribution statement

A. Mangiarotti: Writing – review & editing, Writing – original draft, Visualization, Validation, Software, Project administration, Methodology, Investigation, Funding acquisition, Formal analysis, Data curation, Conceptualization. **A.A. Malafronte:** Resources, Methodology, Investigation, Formal analysis, Data curation. **A.R. Petri:** Methodology, Investigation, Formal analysis, Data curation. **M.N. Martins:** Writing – review & editing, Resources, Methodology, Investigation, Formal analysis, Conceptualization. **J.M. Fernández-Varea:** Writing – review & editing, Writing – original draft, Software, Methodology, Investigation, Formal analysis. **J.P. Peralta:** Software, Investigation, Formal analysis. **A.M.P. Mendez:** Software, Investigation, Formal analysis. **D.M. Mitnik:** Software, Investigation, Formal analysis. **C.C. Montanari:** Writing – review & editing, Writing – original draft, Software, Investigation, Formal analysis.

Declaration of competing interest

The authors declare that they have no known competing financial interests or personal relationships that could have appeared to influence the work reported in this paper.

Acknowledgements

The authors are grateful to Prof. Dr. T. F. Silva and to LAMFI for giving us the foil employed to manufacture the Al target. They are also thankful to Profs. Drs. A. A. F. S. Kerr and H. M. J. Barbosa for granting access to their respective installations (LAPAt and LFA) with micro-analytical scales.

This work has been supported by FAPESP (Fundação de Amparo à Pesquisa do Estado de São Paulo), Brazil Grant No. 2016/13116-5. A. Mangiarotti acknowledges support by CNPq (Conselho Nacional de Desenvolvimento Científico e Tecnológico), Brazil Grants Nos. 306331/2016-0 and 311915/2020-5, A. R. Petri by FAPESP, Brazil Grant No. 2017/12661-2, and J. M. Fernández-Varea by the Spanish MICIU/AEI/10.13039/501100011033, Spain through Grant No. PID2023-147112NB-C22.

[5] The reader wishing to reproduce our calculations should run the `cbethe` program. The `Fortran` source code and the support libraries for atomic properties are available in the supplemental material by Salvat (2022). The default options have been always accepted and the SCSs for protons requested. They are supplied in the `cbethe.dat` file.

J. P. Peralta, A. M. P. Mendez, D. M. Mitnik, and C. C. Montanari acknowledge the financial projects PIP11220200102421CO by Consejo Nacional de Investigaciones Científicas *y* Técnicas, Argentina; Grant No. PICT-2020-SERIE A-01931 by Agencia Nacional de Promoción Científica *y* Tecnológica, Argentina.

Data availability

Data will be made available on request.

References

Abramowitz, M., Stegun, I.A., 1972. Handbook of Mathematical Functions with Formulas, Graphs and Mathematical Tables, ninth ed. Dover, New York.

Ahsan Zeb, M., Kohanoff, J., Sánchez-Portal, D., Arnau, A., Juaristi, J.I., Artacho, E., 2012. Electronic stopping power in Gold: The role of d electrons and the H/He anomaly. Phys. Rev. Lett. 108, 225504.

Badnell, N.R., 2011. A Breit–Pauli distorted wave implementation for autostructure. Comput. Phys. Comm. 182, 1528–1535.

Bak, H.I., Bae, Y.D., Kim, C.S., Kim, M.S., 1994. Measurement of the stopping cross-section of Cu, Ag and Au for 0.2-1.9 MeV He ions. Nucl. Instrum. Methods Phys. Res. B 93, 234–240.

Baker, S., Cousins, R.D., 1984. Clarification of the use of chi-square and likelihood functions in fits to histograms. Nucl. Instrum. Methods Phys. Res. 221, 437–442.

Bar-Shalom, A., Klapisch, M., Oreg, J., 2001. HULLAC, an integrated computer package for atomic processes in plasmas. J. Quant. Spectrosc. Radiat. Transfer 71, 169–188.

Bé, M.-M., Chisté, V., Dulieu, C., Browne, E., Chechev, V., Kuzmenko, N., Helmer, R., Nichols, A., Schönfeld, E., Dersch, R., 2004. Table of Radionuclides. In: Monographie BIPM-5, vol. 2, Bureau International des Poids et Mesures, Pavillon de Breteuil, F-92310 Sévres, France, URL https://www.bipm.org/utils/common/pdf/monographieRI/Monographie_BIPM-5_Tables_Vol2.pdf.

Berger, M.J., Coursey, J.S., Zucker, M.A., Chang, J., 2017. Stopping-Power & Range Tables for Electrons, Protons, and Helium Ions. NIST Standard Reference Database Number 124, National Institute of Standards and Technology, Gaithersburg MD, 20899, URL http://dx.doi.org/10.18434/T4NC7P.

Berger, M.J., Inokuti, M., Andersen, H.H., Bichsel, H., Dennis, J.A., Powers, D., Seltzer, S.M., Turner, J.E., 1984. Report 37: Stopping powers for electrons and positrons. J. Int. Comm. Radiat. Units Meas. (8), os19.

Berger, M.J., Inokuti, M., Andersen, H.H., Bichsel, H., Powers, D., Seltzer, S.M., Thwaites, D., Watt, D.E., 1993. Report 49: Stopping powers and ranges for protons and alpha particles. J. Int. Comm. Radiat. Units Meas. (2), os25.

Bianconi, M., Barradas, N.P., Correra, L., 2005. The stopping cross-section of aluminum for He ions. Nucl. Instrum. Methods Phys. Res. B 239, 127–134.

Bichsel, H., Hiraoka, T., 1992. Energy loss of 70 MeV protons in elements. Nucl. Instrum. Methods Phys. Res. B 66, 345–351.

Bohr, N., 1915. On the decrease of the velocity of swiftly moving electrified particles in passing through matter. Phil. Mag. 30, 581–612.

Bohr, N., 1948. The penetration of atomic particles through matter. Mat. Fys. Medd. Dan. Vid. Selsk. 18 (8), 1–144.

Bortels, G., Collares, F., 1987. Analytical function for fitting peaks in alpha-particle spectra from Si detectors. Int. J. Radiat. Appl. Instrum. Part A 38, 831–837.

Bragg, W.H., Kleeman, R., 1904. On the ionization curves of radium. Proc. R. Soc. Lond. Ser. A 6 10 (55), 726–738.

Bragg, W.H., Kleeman, R., 1905. On the α particles of radium, and their loss of range in passing through various atoms and molecules. Proc. R. Soc. Lond. Ser. A 6 10 (57), 318–340.

Brandt, S., 2014. Data Analysis: Statistical and Computational Methods for Scientists and Engineers, fourth ed. Springer International Publishing, Switzerland.

Brun, R., Rademakers, F., 1997. Root – An object oriented data analysis framework. Nucl. Instrum. Methods Phys. Res. A 389, 81–86.

Bunge, C.F., Barrientos, J.A., Bunge, A.V., 1993. Roothaan-Hartree-Fock ground-state atomic wave functions: Slater-type orbital expansions and expectation values for $Z = 2$–54. At. Data Nucl. Data Tables 53, 113–162.

Correa, A.A., 2018. Calculating electronic stopping power in materials from first principles. Comput. Mater. Sci. 150 (291).

Curie, M., 1900. Les nouvelles substances radioactives et les rayons qu'elles emettent. In: Rapports Présentés au Congres international de Physique. pp. 79–114.

Diwan, P.K., Kumar, S., 2015. dE/dx and range of α-radiations in Al, Ti and Ni metallic foils. Nucl. Instrum. Methods Phys. Res. B 359, 78–84.

Eppacher, C., 1994. Ph.D. thesis, University of Linz. Schriften der Johannes-Kepler-Universität Linz, Universitätsverlag Rudolf Trauner, Linz.

Eppacher, C., Semrad, D., 1992. Dependence of proton and helium energy loss in solids upon plasma properties. Nucl. Instrum. Methods Phys. Res. B 69, 33–38.

Gu, M.F., 2008. The flexible atomic code. Can. J. Phys. 86, 675–689.

Hsu, J.Y., Yu, Y.C., Liang, J.H., Chen, K.M., 2005. Experimental stopping forces in aluminum and silver by ^{3}He/^{4}He, ^{6}Li/^{7}Li and ^{10}B/^{11}B ions. Nucl. Instrum. Methods Phys. Res. B 241, 155–159.

Hsu, J.Y., Yu, Y.C., Liang, J.H., Chen, K.M., Niu, H., 2004. Energy loss of He, Li and B isotopes with MeV energies in Au. Nucl. Instrum. Methods Phys. Res. B 219–220, 251–255.

James, F., Roos, M., 1975. Minuit – a system for function minimization and analysis of the parameter errors and correlations. Comput. Phys. Comm. 10, 343–367.

Kumar, S., Diwan, P.K., 2015. Energy loss and straggling of α-particles in Ag and Sn metallic foils. J. Radiat. Res. Appl. Sci. 8, 538–543.

Kumar, S., Diwan, P.K., 2018. Energy loss and range of α-particles in different metallic foils. Radiat. Eff. Defects Solids 173, 970–977.

Levine, Z.H., Louie, S.G., 1982. New model dielectric function and exchange–correlation potential for semiconductors and insulators. Phys. Rev. B 25, 6310–6316.

L'Hoir, A., 1984. Study of the asymmetrical response of silicon surface barrier detectors to MeV light ions. Application to the precise analysis of light ions energy spectra. I. Helium ions. Nucl. Instrum. Methods Phys. Res. 223, 336–345.

Mangiarotti, A., Lauth, W., Jakubassa-Amundsen, D.H., Klag, P., Malafronte, A.A., Martins, M.N., Nielsen, C.F., Uggerhøj, U.I., 2021a. Spectral distribution and Coulomb correction for nuclear bremsstrahlung induced by heavy targets. Phys. Lett. B 815, 136113.

Mangiarotti, A., Petri, A.R., Malafronte, A.A., Gonçalves, J.A.C., Barros, S.F., Bueno, C.C., Fernández-Varea, J.M., Maidana, N.L., Martins, M.N., Vanin, V.R., 2021b. A low-cost small-size commercial PIN photodiode: II. comparison of measurements with monoenergetic electrons to analytical expressions and Monte Carlo simulations. Radiat. Phys. Chem. 182, 109102.

Markin, S., 2007. Dissertation. Johannes-Kepler-Universität Linz, Linz.

Markin, S.N., Primetzhofer, D., Spitz, M., Bauer, P., 2009. Electronic stopping of low-energy H and He in Cu and Au investigated by time-of-flight low-energy ion scattering. Phys. Rev. B 80, 205105.

Martínez-Tamayo, G., Eckardt, J.C., Lantscher, G.H., Arista, N.R., 1996. Energy loss of H^+ and He^+ in Al, Zn, and Au in the very low- to intermediate-energy range. Phys. Rev. A 54, 3131.

Mendez, A.M.P., Montanari, C.C., Mitnik, D.M., 2019. Relativistic atomic structure calculations of heavy targets for inelastic collisions. Nucl. Instrum. Methods Phys. Res. B 460, 114–118.

Mermin, N.D., 1970. Lindhard dielectric function in the relaxation-time approximation. Phys. Rev. B 2362–2363.

Montanari, C.C., 2025. Electronic Stopping Power of Matter for Ions Graphs, Data, Comments, and Programs, 1928–2025. https://www-nds.iaea.org/stopping/.

Montanari, C.C., Dimitriou, P., 2017. The IAEA stopping power database, following the trends in stopping power of ions in matter. Nucl. Instrum. Methods Phys. Res. B 408, 50–55.

Montanari, C.C., Dimitriou, P., Marian, L., Mendez, A.M.P., Peralta, J.P., Bivort-Haiek, F., 2024. The IAEA electronic stopping power database: Modernization, review, and analysis of the existing experimental data. Nucl. Instrum. Methods Phys. Res. B 551, 165336.

Montanari, C.C., Miraglia, J.E., 2013. The dielectric formalism for inelastic processes in high-energy ion–matter collisions. In: Belkić, D. (Ed.), Advances in Quantum Chemistry: Theory of Heavy Ion Collision Physics in Hadron Therapy. Vol. 2, Elsevier, New York, pp. 165–201, Ch. 7.

Moro, M.V., Silva, T.F., Mangiarotti, A., Guimarães-Filho, Z.O., Rizzutto, M.A., Added, N., Tabacniks, M.H., 2016. Traceable stopping cross sections of Al and Mo elemental targets for 0.9–3.6-MeV protons. Phys. Rev. A 93, 022704.

Moroz, L., Baratta, G., Strazzulla, G., Starukhina, L., Dotto, E., Barucci, M.A., Arnold, G., Distefano, E., 2004. Optical alteration of complex organics induced by ion irradiation: 1. Laboratory experiments suggest unusual space weathering trend. Icarus 170, 214–228.

Moussa, D., Damache, S., Ouichaoui, S., 2015. Accurate stopping power measurements for (0.21-2.68) MeV/u $^{1}H^{+}$ and $^{4}He^{+}$ ions crossing thin Al foils; extraction of the (I, b) parameters. Nucl. Instrum. Methods Phys. Res. B 343, 44–47.

Navas, S., Amsler, C., Gutsche, T., Hanhart, C., Hernández-Rey, J.J., Lourenço, C., Masoni, A., Mikhasenko, M., Mitchell, R.E., et al., 2022. Review of particle physics. Phys. Rev. D 110, 030001.

Pascual-Izarra, C., Barradas, N.P., 2008. Introducing routine pulse height defect corrections in IBA. Nucl. Instrum. Methods Phys. Res. B 266, 1866–1870.

Paul, H., 2003. Judging the reliability of stopping power tables and programs for heavy ions. Nucl. Instrum. Methods Phys. Res. B 209, 252–258.

Peralta, J.P., Fiori, M., Mendez, A.M.P., Montanari, C.C., 2022. Stopping power calculations and the Levine-Mermin dielectric function for inner shells. Phys. Rev. A 105, 062814.

Peralta, J.P., Mendez, A.M.P., Mitnik, D.M., Montanari, C.C., 2023. Systematic study of the stopping power of the lanthanides. Phys. Rev. A 107, 052809.

Piessens, R., Doncker-Kapenga, E.D., Überhuber, C.W., Kahaner, D.K., 1983. Quadpack: A Subroutine Package for Automatic Integration. Springer Verlag, Berlin, Germany.

Press, W.H., Flannery, B.P., Teukolsky, S.A., Vetterling, W.T., 1992. Numerical Recipes in FORTRAN 77, the Art of Scientific Computing, second ed. Cambridge University Press, Cambridge, England.

Primetzhofer, D., 2012. Inelastic energy loss of medium energy H and He ions in Au and Pt: Deviations from velocity proportionality. Phys. Rev. B 86, 094102.

Primetzhofer, D., Rund, S., Roth, D., Goebl, D., Bauer, P., 2011. Electronic excitations of slow ions in a free electron gas metal: Evidence for charge exchange effects. Phys. Rev. Lett. 107, 163201.

Räisänen, J., Rauhala, E., Björnberg, M., Kiss, A.Z., Dominguez, J., 1991. Stopping powers of Al and Sn for ^{4}He, ^{7}Li, ^{11}B, ^{12}C, ^{14}N and ^{16}O ions in the energy range 0.5–2.6 MeV/amu. Radiat. Eff. Defects Solids 118, 97–103.

Reichmuth, A., 2001. Adverse Influences and their Prevention in Weighing. Mettler Toledo, Switzerland.

Rutherford, E., 1906. Retardation of the α particle from radium in passing through matter. Proc. R. Soc. Lond. Ser. A 6 8 (48), 134–146.

Sakamoto, N., Ogawa, H., Mannami, M., Kimura, K., Susuki, Y., Hasegawa, M., Hatayama, I., Noro, T., Ikegami, H., 1991. Stopping powers of metallic elements for high energy ions. Radiat. Eff. Defects Solids 117, 193–195.

Salonen, E., Nordlund, K., Keinonen, J., Wu, C.H., 2000. Bond-breaking mechanism of sputtering. Europhys. Lett. 52, 504–510.

Salvat, F., 2022. Bethe stopping-power formula and its corrections. Phys. Rev. A 106, 032809.

Salvat, F., Barjuan, L., Andreo, P., 2022. Inelastic collisions of fast charged particles with atoms: Bethe asymptotic formulas and shell corrections. Phys. Rev. A 105, 042813.

Semrad, D., Eppacher, C., Tober, R., 1990. The stopping power of Ag and Au, with regard to higher-order Z_1-effects. Nucl. Instrum. Methods Phys. Res. B 48, 79–82.

Shiomi-Tsuda, N., Sakamoto, N., Ishiwari, R., 1994. Stopping powers of Be, Al, Ti, V, Fe, Co, Ni, Cu, Zn, Mo, Rh, Ag, Sn, Ta, Pt, and Au for 13 MeV deuterons. Nucl. Instrum. Methods Phys. Res. B 93, 391–398.

Sillanpää, J., Vainonen-Ahlgren, E., Haussalo, P., Keinonen, J., 1996. Stopping of 5-100 keV helium in molybdenum, chromium, copper and nickel. Nucl. Instrum. Methods Phys. Res. B 54, 1–8.

Trzaska, W.H., Knyazheva, G.N., Perkowski, J., Andrzejewski, J., Khlebnikov, S.V., Kozulin, E.M., Malkiewicz, T., Mutterer, M., Savelieva, E.O., 2018. New experimental stopping power data of ^{4}He, ^{16}O, ^{40}Ar, ^{48}Ca and ^{84}Kr projectiles in different solid materials. Nucl. Instrum. Methods Phys. Res. B 418, 1–12.

Trzaska, W.H., Lyapin, V., Alanko, T., Mutterer, M., Räisänen, J., Tjurin, G., Wojdyr, M., 2002. New approach to energy loss measurements. Nucl. Instrum. Methods Phys. Res. B 195, 147–165.

Ullah, R., Artacho, E., Correa, A.A., 2018. Core electrons in the electronic stopping of heavy ions. Phys. Rev. Lett. 121, 116401.

Varelas, C., Biersack, J., 1970. Reflection of energetic particles from atomic or ionic chains in single crystals. Nucl. Instrum. Methods 79, 213–218.

Werner, W.S.M., Glantschnig, K., Ambrosch-Draxl, C., 2009. Optical constants and inelastic electron-scattering data for 17 elemental metals. J. Phys. Chem. Ref. Data 38, 1013–1092.

Williams, G., 2015. X-Ray Data Booklet, Section 1.1: Electron Binding Energies. http://xdb.lbl.gov/Section1/Sec_1-1.html.

Zhang, Y., Weber, W.J., Razpet, A., Possnert, G., 2005. Electronic stopping powers for He, Be and F ions in Au. Nucl. Instrum. Methods Phys. Res. B 227, 479–484.

Ziegler, J.F., 2004. SRIM-2003. Nucl. Instrum. Methods Phys. Res. B 219–220, 1027–1036.

Ziegler, J.F., Biersack, J.P., Littmark, U., 1985. The Stopping and Range of Ions in Solids, first ed. Pergamon Press, Oxford.

Ziegler, J.F., Ziegler, M.D., Biersack, J.P., 2010. SRIM – the stopping and range of ions in matter (2010). Nucl. Instrum. Methods Phys. Res. B 268, 1818–1823.

Zinkle, S.J., Skuratov, V.A., Hoelzer, D.T., 2002. On the conflicting roles of ionizing radiation in ceramics. Nucl. Instrum. Methods Phys. Res. B 191, 758–766.